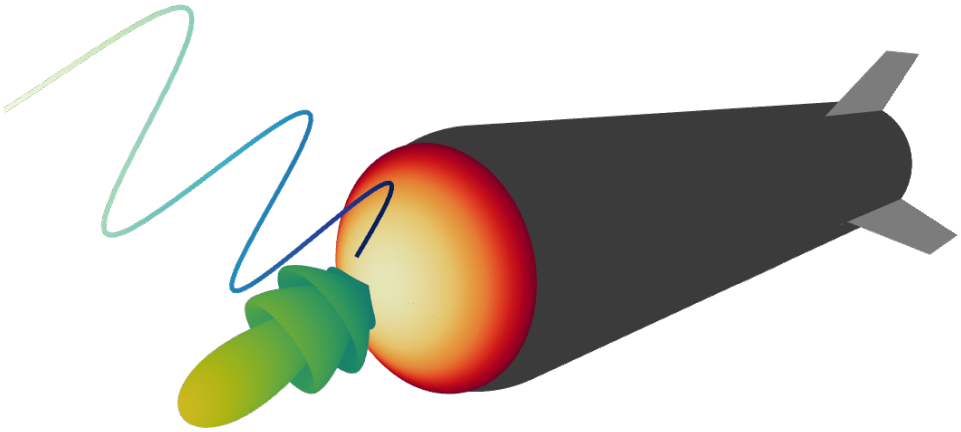

Electromagnetic modeling of the effect of plasma sheath on radar signatures of hypersonic targets

Thesis for the degree of Master of Science in Physics

LIAM ANTONSSON

DEPARTMENT OF PHYSICS

CHALMERS UNIVERSITY OF TECHNOLOGY
Gothenburg, Sweden 2025
www.chalmers.se

Master's thesis 2025

Electromagnetic modeling of the effect of plasma sheath on radar signatures of hypersonic targets

LIAM ANTONSSON

CHALMERS
UNIVERSITY OF TECHNOLOGY

Department of Physics
Chalmers University of Technology
Gothenburg, Sweden 2025

Electromagnetic modeling of the effect of plasma sheath on radar signatures of hypersonic targets
LIAM ANTONSSON

Supervisor: Andréas Sundström, Saab
Examiner: István Pusztai, Department of Physics

Master's Thesis 2025
Chalmers University of Technology
Department of Physics
SE-412 96 Gothenburg
Telephone +46 31 772 1000

Cover: Visualization designed in `matcha.io` showing the scattering of a microwave pulse from a plasma-coated missile.

Typeset in LaTeX
Printed by Chalmers Reproservice
Gothenburg, Sweden 2025

Electromagnetic modeling of the effect of plasma sheath on radar signatures of hypersonic targets
LIAM ANTONSSON
Department of Physics
Chalmers University of Technology

Abstract

Hypersonic missiles have been suggested to have significantly different radar signatures compared to similar slower vehicles. This has been attributed to the plasma sheath that forms when high-temperature air in the hypersonic shock front partially ionizes air molecules. Under certain conditions, the free electrons in this plasma can absorb electromagnetic radiation. It is unclear whether this effect could dampen the scattered radiation from targeted hypersonic missiles, effectively making them stealthy to radar. The physics of plasma-induced stealth of hypersonic vehicles is quite complex, involving the spatial distributions of plasma and electron–neutral collision frequencies as well as the microwave frequency. For this reason, broad claims about the stealth of hypersonic vehicles must be supported by accurate numerical simulations.

In this thesis, the effects of a thin plasma sheath have been studied in various settings and geometries with the aid of electromagnetic as well as hydrodynamic simulations. The ability of a plasma to shield rough surfaces, which otherwise have a large radar signature, was investigated by simulating the electromagnetic wave scattering of a plasma-covered metal slab with surface roughness in a 2D geometry. Somewhat unexpectedly, the plasma did not behave like a mirror for low frequencies and when the radiation was expected to be attenuated, it was instead amplified. Additionally, the ability of the plasma sheath to distort scattered electromagnetic waves was studied analytically. The distortion was exaggerated in this simple model compared to a real-world scenario, but even so, it was negligible for almost every frequency and can therefore be neglected. Finally, to study the effect of a plasma sheath with a realistic plasma density, the plasma frequency and collision frequency distributions were computed for a metal sphere flying at speeds of 3–5 $\mathrm{km\,s^{-1}}$ in an ambient pressure representative of a 40 km altitude. While the calculated radar signature has a limited accuracy below 1 GHz, we can conclude that in that frequency range the presence of the plasma sheath can either increase or reduce the radar signal, depending on the frequency. At some frequencies the decrease was as large as 10 dB. Our results also indicate that the plasma sheath only has minor effects on the radar signatures of hypersonic vehicles traveling below 3 $\mathrm{km\,s^{-1}}$, for the microwave bands above 1 GHz.

Keywords: radar, plasma, hypersonic, electromagnetic simulation, computational fluid dynamics simulation.

Acknowledgements

I would like to express my gratitude to Andréas Sundström, at the Future-technologies group at Saab Surveillance, and István Pusztai, at the Plasma Theory Research Group at Chalmers, for all the support in this endeavor. Without the fruitful discussions we had and feedback they provided, this thesis would not have materialized. I also extend my gratitude to Saab for proposing such an interesting research topic and for providing an excellent research environment to work in.

Liam Antonsson, Gothenburg, June 2025

List of Acronyms

Below is the list of acronyms that have been used throughout this thesis listed in alphabetical order:

BRCS	Bistatic radar cross-section
CFD	Computational-fluid-dynamics
EM	Electromagnetic
FDTD	Finite-difference time-domain
FM	Frequency modulation
FWHM	Full-width-at-half-maximum
LFM	Linear frequency modulation
PEC	Perfect electric conductor
PML	Perfectly matched layer
RCS	Radar cross-section
SBR	Shooting and bouncing rays

Nomenclature

Below is the nomenclature of variables that have been used throughout this thesis.

σ_{RCS}	Radar cross-section
σ_{BRCS}	Bistatic radar cross-section
R	Range
f	Frequency
B	Bandwidth
L_{tot}	Total loss
L_{E}	Loss due to plasma absorption
L_{MM}	Loss due to mismatch
r	Sphere radius
f_{p}	Plasma frequency
f_{c}	Collision frequency
$\bar{\Omega}_{e-i}^{(1,1)}$	Collisional integral for electron and other species pair
$\hat{\varepsilon}$	Relative permittivity
ρ	Reflectance
$\mathcal{F}$	Fourier transform

Contents

1

Introduction

Hypersonic missiles traveling at speeds of Mach 5–25 (∼1500–7500 m/s) have existed for a long time. However, fairly recently, the Russian-developed *Zircon* has demonstrated the feasibility of *maneuverable* hypersonic missiles traveling at lower altitudes [1]. A key advantage of these missiles for the attacker is the shrunken response time available for the defender to detect, classify and deploy countermeasures. Furthermore, the missiles can be used for deception by initially being launched in one direction targeting one region and then switching direction mid-flight to target another region. It has been shown that for certain missiles, targets beyond 3300 km crossrange can be hit provided a distance of 5000 km downrange [2]. To this end, it is critical to detect hypersonic weapon systems as early as possible to mitigate damage.

Radar is a common tool for detecting airborne threats, which is based on the directed emission of microwave pulses at targets. The most important piece of hardware in a radar is the antenna. In a monostatic radar, this antenna has two functions, transmitting and receiving microwaves, whereas in a bistatic radar, these functions are handled by separate antennas that are spatially separated. The first objective of the antenna is to send out microwaves to impinge upon objects obstructing the field of view of the antenna such that the radiation gets scattered. The second objective of the antenna is then to receive and collect the backscattered radiation. By correlating the transmitted and received radiation, a time of flight t can be identified for each pulse. The radial distance of a potential target can then be inferred to be $R = ct/2$ in the special case of a monostatic radar. In order to distinguish a potential target from background noise, the backscattered radiation must be sufficiently strong. In a radar system, this surveillance is done continuously, enabling it to constantly monitor the surrounding airspace. In modern radar technology, information regarding radial velocity and radar cross-section (RCS) can also be inferred by post-processing the backscattered radiation. For this reason it is crucial that the received measurements are accurate in order to not just locate targets but also recognize and predict their actions.

To make the data acquisition as difficult as possible, adversaries are constantly adapting to each other's measuring techniques by developing appropriate jamming techniques or other indirect stealth technologies. One physical phenomenon for hypersonic missiles that has been suggested to be useful for stealth is the generation

of a so-called *plasma sheath*. The plasma sheath is a region in the hydrodynamic shock front partly composed of free electrons. These electrons are generated near the front surface of the missiles as a result of chemical reactions and ionization in the air due to the immense temperature and pressure inside the shockwave.

The plasma–microwave interaction is complex, depending on missile speed and geometry, ambient pressure and frequency. It is, however, of fundamental interest to understand this interaction in order to make radar systems versatile to all types of missiles. The extent to which the plasma sheath affects the radar signature is debated and is currently ongoing research [1, 3]. Nevertheless, it is unlikely that the plasma sheath acts like a complete radar cloak, as some sources have suggested [1], absorbing all radiation and therefore rendering the missile undetectable to radar systems.

The openly published research on this matter is primarily composed of numerical studies, with limited experimental data for validating the simulations. Although some open experimental research has been performed [3], it remains scarce. The main focus of numerical studies is the RCS and how this changes when a plasma covers a target. However, as Xu *et al.* [4] pointed out in one of their numerical studies, the scattered microwave also becomes distorted, which has the potential for being detrimental for the *pulse-compression* step of signal processing. This step involves the correlation between the delayed signal or the matched filter to increase the range resolution or signal strength. In the case of a distorted radar echo, a mismatch loss is introduced [4], which is discussed in more detail in section 2.1.2. The distortion comes primarily in the form of frequency-dependent microwave absorption by the plasma.

A common numerical technique for studying the scattering of microwaves around objects is finite-difference time-domain (FDTD) simulations. In these simulations, Maxwell's equations are solved on a spatial grid and propagated throughout time. Due to its widespread use, there exist many open and efficient FDTD solvers online for electromagnetic simulation. As such, this technique is suitable for modeling the scattering of microwaves, given the scope of this project. This method does not, however, address the problem of determining the shape and characteristics of the plasma sheath itself. To model that with reasonable accuracy, the Navier–Stokes equations need to be solved for an atmospheric medium containing several gases. The chemical reactions of these gases at hypersonic conditions must also be modeled in order to quantify the generation of free electrons, acting as a plasma sheath. Thankfully, there exist solvers for this computational-fluid-dynamics (CFD) problem online as well. Therefore, the methods used for this project can be split up into two parts. First, the use of a CFD solver for determining a realistic plasma sheath. Second, the use of a FDTD solver for determining the scattered microwaves. The analysis will, however, be centered around the latter.

To investigate the effects of the plasma sheath the following questions have been studied to various depth:

- What is the effect of a thin, i.e., thinner than the radar wavelength, plasma sheath at oblique incidence for a planar surface with random roughness?
- How significant is the distortion induced by the plasma for pulse-compressed waveforms?
- What are reasonable plasma parameters for a naturally generated plasma from hypersonic shock heating? What are the expected electron-density profiles and the electron–neutral collision frequency?
- How large are the scattering amplitudes at monostatic and bistatic setups, i.e., scattering amplitudes in all directions, affected by the plasma sheath for a reflective metal sphere?

1.1 Thesis outline

The theoretical background necessary to obtain the results in this thesis is presented in chapter 2. Initially, some background regarding basic radar signatures and their post-processing is described. Thereafter a weakly ionized atmosphere is described, together with characteristic frequencies of plasmas in this context. Electromagnetic wave propagation is then discussed in these plasmas and a 1D model for the wave reflectance is presented.

In chapter 3, the numerical tools *hy2Foam* and *meep*, used to derive the results presented in the thesis are explained. Relevant settings for reproducing the results are also provided. The results are presented in chapter 4. Four different scenarios are analyzed. One scenario is a simplified 1D model for the scattering from a plasma-covered perfect electric conductor (PEC) slab. Another scenario involves the scattering from a plasma-covered rough surface. The next scenario covers the distortion of the scattered radiation for a plasma-covered PEC slab. Lastly, the scattering of a plasma-covered PEC sphere is analyzed with realistic plasma and collision frequencies. Finally, in chapter 5, the conclusions are summarized alongside an outlook for future work.

2

Theoretical background

In this chapter, basic radar physics and the post-processing of signals relevant to this project are described. The principles of a weakly ionized plasma, by atmospheric thermal heating, are also outlined and discussed.

2.1 Basic radar physics

This section covers the working principles of radar physics and basic post-processing for the received signal necessary for this project. In addition, an analytic solution for the scattering of a PEC sphere is briefly described.

2.1.1 Radar signature

The purpose of radar systems is to detect and measure the distance and velocity of targets relative to a transmitter and receiver of electromagnetic radiation. It is based upon the principle that all objects scatter radiation. Monostatic radars are specifically designed to emit microwave pulses at targets with a transmitting antenna and measure the backscattered radiation with a receiving antenna. In monostatic systems, the transmitter and receiver are collocated. By utilizing the time of flight of the signal, the Doppler shift caused by moving targets and the strength of the received signal, information about the location, velocity and size of the target can be inferred. This can in theory be done at any frequency, but to avoid unwanted clutter signals, such as small particles of rain droplets, the wavelength must be longer than a few millimeters. For this reason, most radar systems operate within the microwave band 1–10 GHz. This band also has the advantage of not being polluted by sunlight and thermal radiation from the ground.

One limiting factor for detecting targets is the received power, which for a monostatic radar, can be determined with the radar range equation

$$P_{\mathrm{r}} = \frac{P_{\mathrm{t}} G_{\mathrm{t}}}{4\pi R^2} \frac{\sigma_{\mathrm{RCS}}}{4\pi R^2} A_{\mathrm{e}}, \tag{2.1}$$

where P_{t} denotes the emitted power, $G_{\mathrm{t}} \sim 4\pi A_{\mathrm{e}}/\lambda^2$ is the gain of the transmitting antenna, σ_{RCS} is the RCS, A_{e} is the effective aperture of the receiving antenna, R is the distance to the target and λ is the carrier wave wavelength of the microwave. The

first fraction, $P_t G_t / 4\pi R^2$, represents the intensity of the transmitted pulse at the target, while $\sigma_{RCS}/4\pi R^2$ represents the fraction of that pulse that is backscattered to the receiver. Here, it is assumed that $R \gg D^2/\lambda$, or more simply $R \gg G_t\lambda$ for a symmetric antenna, where D is the greatest length of the antenna. This assumption makes sure that the far-field approximation is accurate at both ends and the pulses can be approximated as plane waves. The RCS is defined as

$$\sigma_{RCS}(\alpha) = \lim_{R\to\infty} 4\pi R^2 \frac{|E_s(R, \theta = 180°, \alpha)|^2}{|E_i|^2}, \tag{2.2}$$

for the incident electric field strength E_i and backscattered electric field strength $E_s(R, \theta = 180°)$. The aspect angle α denotes the angle the target makes with the incident field with respect to some reference orientation. In general, α is a tuple of two angles, elevation and azimuth, but in this project only a single angle will be of interest and this will be chosen such that the incident field encounters as much of the plasma as possible. For similar reasons only a single bistatic angle θ will be considered, despite it being a tuple of two angles, the elevation and azimuth. The bistatic angle is the angle subtended by the transmitter, object and receiver in a bistatic setup. For angles, θ, other than 180° the bistatic radar cross-section (BRCS) is recovered

$$\sigma_{BRCS}(\theta, \alpha) = \lim_{R\to\infty} 4\pi R^2 \frac{|E_s(R, \theta, \alpha)|^2}{|E_i|^2}. \tag{2.3}$$

In figure 2.1, a schematic is shown for a target rotated by an angle α, with its BRCS plotted in blue as it is being passed by a plane wave propagating in the direction of the dashed arrow. The BRCS is relevant in a bistatic radar system, where the transmitter and receiver are placed at different locations. The RCS and BRCS depend on the shape of the target, its surface material, the orientation of the object and the frequency of the incoming radiation.

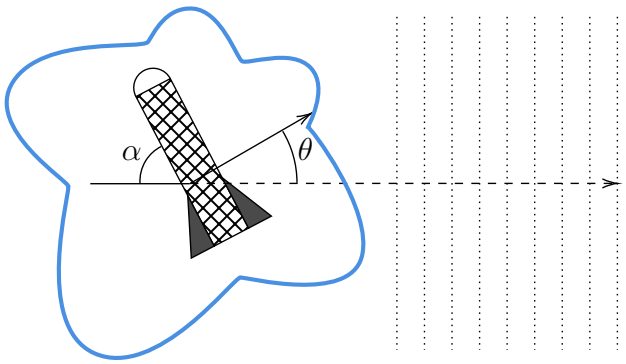

Figure 2.1: Schematic polar plot of the BRCS, in blue, dependent on the angle θ, relative to the incident wave marked with dashed lines. The target is rotated by an aspect angle α.

2.1.2 Pulse compression in radar

Pulse compression is a technique for improving the range resolution, or reducing the uncertainty in the position of detected objects, while keeping a fixed pulse duration for a radar system. This is done by coding the modulation of the transmitted pulse and then correlating the received echoes with the known transmitted pulse code. To illustrate the effect of the pulse coding or modulation, the correlation output of two differently modulated signals will be shown. First, a constant frequency signal is used and then a frequency modulated (FM) signal. In an ideal simple pulse, with carrier frequency f and pulse length T the emitted signal at time t has an electric field strength [5]

$$s(t) \propto \begin{cases} \mathrm{e}^{2\pi \mathrm{i} f t}, -\frac{T}{2} < t < \frac{T}{2} \\ 0, \text{otherwise.} \end{cases} \tag{2.4}$$

The reflected signal $r(t)$ is then in the ideal case, without a plasma, just a time-shifted and attenuated copy of the emitted signal, assuming a noise-free environment. The signal arrives at the receiver at a later time $t_0 = 2R/c$, where R is the distance. By performing complex correlation between the emitted and received signals, the obtained pulse-compression amplitude is

$$\begin{aligned} y(t) &= \langle s(\tau), r(\tau) \rangle (t) \propto \langle s(\tau), s(\tau - t_0) \rangle (t) = \int_{-\infty}^{\infty} s(\tau) \bar{s}(\tau + t - t_0) \, \mathrm{d}\tau \\ &\propto \Lambda \left(\frac{t - t_0}{T} \right) \mathrm{e}^{2\pi \mathrm{i} f (t - t_0)}, \text{where} \end{aligned} \tag{2.5}$$

$$\Lambda(x) = \max(0, 1 - |x|), \tag{2.6}$$

for a distant target, where $y(t)$ has a peak at t_0 and B is the bandwidth. Using the peak of the correlated signal, the position of the target can be located by calculating $R = ct_0/2$. The disadvantage of using this simple pulse is that the width, often defined as the full-width-at-half-maximum (FWHM) or simply $-3\,\mathrm{dB}$ width, of $y(t)$ is proportional to the pulse length T, which we want to keep long to emit as much energy as possible. Thus, increasing the pulse length increases the emitted energy but also increases the uncertainty in the position, if no intra-pulse coding or modulation is used.

For effective pulse compression, FM signals are often used. In this case, using the same assumptions as above for a linearly modulated signal (LFM) [5]

$$s(t) \propto \begin{cases} \mathrm{e}^{2\pi \mathrm{i} \left((f - \frac{B}{2}) t + \frac{B}{2T} t^2 \right)}, -\frac{T}{2} < t < \frac{T}{2} \\ 0, \text{otherwise.} \end{cases} \tag{2.7}$$

The pulse-compressed signal is then given by

$$\begin{aligned} y(t) &= \langle s(\tau), r(\tau) \rangle (t) \propto \langle s(\tau), s(\tau - t_0) \rangle (t) \\ &\propto \Lambda \left(\frac{t - t_0}{T} \right) \operatorname{sinc} \left(B t \Lambda \left(\frac{t}{T} \right) \right) \mathrm{e}^{2\pi \mathrm{i} f (t - t_0)}, \text{where} \end{aligned} \tag{2.8}$$

$$\operatorname{sinc}(x) = \frac{\sin(\pi x)}{\pi x}. \tag{2.9}$$

Now the length of the main lobe of $y(t)$ is approximately $1/B$, independent of T. Therefore, we can use a wide bandwidth to get a fine range resolution.

A target cloaked with a plasma will have the received signal either increased, decreased or distorted, depending on the plasma profile and the swept frequencies, due to the frequency-dependent permittivity of the plasma. The detection strength can be quantified with $Y(t) = |y(t)|^2$. To evaluate the impact of the plasma coating on the peak of $Y(t) = |y(t)|^2$, the loss L_{tot} will be considered,

$$L_{\text{tot}} = L_{\text{E}} L_{\text{MM}} \tag{2.10}$$

$$L_{\text{tot}} = \frac{\max\limits_t \left[Y_{\text{plasma}}(t)\right]}{\max\limits_t \left[Y_{\text{no plasma}}(t)\right]} \tag{2.11}$$

$$L_{\text{E}} = \frac{\int Y_{\text{plasma}}(t)\,\mathrm{d}t}{\int Y_{\text{no plasma}}(t)\,\mathrm{d}t}, \tag{2.12}$$

where L_{E} symbolizes the losses due to the energy absorption by the plasma. The mismatch loss, L_{MM}, represents the losses caused by the difference in the signal shape between the emitted and received signals [4].

2.1.3 Mie scattering

While the RCS and BRCS of a general shape are complicated to compute, they can be computed by approximating every point on the surface as a point scatterer and summing up the contributions from each point. This can be done numerically, but for shapes like a sphere, there exist analytical solutions of the RCS and BRCS. The scattering of electromagnetic plane waves by spheres in a vacuum is known as Mie scattering. For a PEC sphere with radius r and plane wave with frequency f, the normalized RCS and BRCS are [6]

$$\frac{\sigma_{\text{BRCS}}}{\pi r^2} = \frac{c^2}{4\pi^2 f^2 r^2}\left(|A_{\theta_1}|^2 \cos^2\theta_2 + |A_{\theta_2}|^2 \sin^2\theta_2\right) \tag{2.13}$$

$$\sigma_{\text{RCS}} = \sigma_{\text{BRCS}}(\theta_1 = 180^\circ), \tag{2.14}$$

where θ_1 and θ_2 are the bistatic polar and azimuthal angles, respectively, with respect to the propagation direction of the plane wave. The geometry is illustrated in figure 2.2. Here it was assumed that the incident wave is linearly polarized in the y-direction and propagates in the x-direction. The A_{θ_1} and A_{θ_2} terms in equation (2.13) contain information about the polarization and they are defined as

$$|A_{\theta_1}|^2 = \left|\sum_{n=1}^{\infty} b_n \sin\theta_1 P_n^{1'}(\cos\theta_1) - c_n \frac{P_n^1(\cos\theta_1)}{\sin\theta_1}\right|^2 \tag{2.15}$$

$$|A_{\theta_2}|^2 = \left|\sum_{n=1}^{\infty} b_n \frac{P_n^1(\cos\theta_1)}{\sin\theta_1} - c_n \sin\theta_1 P_n^{1'}(\cos\theta_1)\right|^2, \tag{2.16}$$

where P_n^m is the associated Legendre polynomial at order n. The coefficients a_n, b_n and c_n are defined as

$$a_n = \frac{2n+1}{n(n+1)} \tag{2.17}$$

$$b_n = -a_n \frac{j_n^{'}(2\pi fr/c)}{h_n^{(2)'}(2\pi fr/c)} \tag{2.18}$$

$$c_n = -a_n \frac{j_n(2\pi fr/c)}{h_n^{(2)}(2\pi fr/c)}, \tag{2.19}$$

$$\tag{2.20}$$

for the spherical Bessel function, j_n, of first kind at order n and the spherical Hankel function, $h_n^{(2)}$, of second kind at order n.

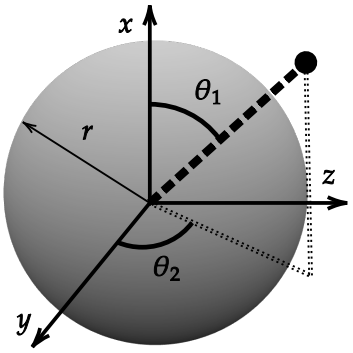

Figure 2.2: Schematic of a PEC sphere with radius r and its bistatic polar and azimuthal angles θ_1 and θ_2.

2.2 Plasma physics

This section covers the relevant principles of weakly ionized atmospheric plasmas in the lower atmosphere when thermally heated. In addition, the electromagnetic wave propagation in a plasma is described and a 1D model of a plasma-covered slab is discussed.

2.2.1 Atmospheric plasmas

Plasma is a state of matter composed of a significant proportion of free charged particles, namely electrons and ions. The free and charged particles make a plasma susceptible to an electromagnetic field, despite being macroscopically electrically neutral. In the atmosphere, gas particles can be ionized by a sufficiently strong electric field, such as in lightning, or by heating up gas to a sufficient temperature that the thermal energy of collisions ionize the gas molecules. When doing the latter at timescales much longer than the collision time of molecules the gas can be considered to be in chemical equilibrium [7]. In atmospheric conditions, it is actually not O_2 or N_2 molecules that ionize first, but rather NO [7]. Simulations

have shown that the most important reactions for the generation of an atmospheric plasma at temperatures $T < 9000\,\mathrm{K}$ [7] are

$$\begin{aligned} &\mathrm{O_2 + M \leftrightarrow 2O + M},\\ &\mathrm{N_2 + M \leftrightarrow 2N + M},\\ &\mathrm{NO + M \leftrightarrow N + O + M},\\ &\mathrm{NO + O \leftrightarrow O_2 + N},\\ &\mathrm{N_2 + O \leftrightarrow NO + N},\\ &\mathrm{N + O \leftrightarrow NO^+ + e^-}. \end{aligned} \tag{2.21}$$

Only seven species need to be considered: $\mathrm{O_2}$, $\mathrm{N_2}$, O, N, NO, $\mathrm{NO^+}$ and e^- in order to model the plasma formation [7]. The introduction of the species denoted by M, is a trick to reduce the number of written reactions, as M can be substituted by any of the seven species. For the speeds of projectiles considered in this project, the temperature never exceeds 9000 K.

Figure 2.3a shows the number densities of the seven species at different temperatures of a gas that is heated isobarically at a pressure of 101.3 kPa and initially composed of 21 % $\mathrm{O_2}$ and 79 % $\mathrm{N_2}$. The data has been taken from the *Cantera* package [8]. Although, this does not provide an accurate estimate for the chemical composition at the front of hypersonic projectiles, as the pressure is not held constant and the surrounding medium is in chemical non-equilibrium. However, it can serve as a reference point to compare species concentrations.

2.2.2 Characteristic frequencies

In an ideal quasineutral plasma at thermal equilibrium, displacing a slab of electrons creates a restoring electrostatic force. This, in turn, causes the electrons to oscillate at a frequency f_p, known as the plasma frequency, which can be shown to be

$$f_\mathrm{p} = \frac{1}{2\pi}\sqrt{\frac{n_e e^2}{m_e \varepsilon_0}}, \tag{2.22}$$

in the case of cold electrons moving much slower than the speed of light and ions moving considerably slower than electrons. The electron density is denoted by n_e, while the elementary charge is e, the electron mass is m_e and vacuum permittivity is ε_0.

Electrons in a plasma will also collide with other particles. The corresponding frequency f_c is known as the electron collision frequency and in the case of the seven-species model considered in section 2.2.1 this frequency can be determined from

$$f_\mathrm{c} = \sum_{i=1}^{7} n_i \bar{v}_e \pi \bar{\Omega}_{e-i}^{(1,1)} \tag{2.23}$$

$$\bar{v}_e = \sqrt{\frac{8 k_b T_e}{\pi m_e}}, \tag{2.24}$$

where the index i denotes the species, n_i, $\bar{v_e}$ and T_e are the species density, average speed of the electrons and electron temperature, respectively. For small electron densities, f_c is essentially the electron-neutral collision frequency f_c^{e-n}. In this project, T_e has been set to T_t, the translational component of the temperature. The collisional integral, or the average cross section, $\pi\bar{\Omega}_{e-i}^{(1,1)}$ has the empirically derived relationship

$$\frac{\pi\bar{\Omega}_{e-i}^{(1,1)}}{\text{Å}^2} = \tilde{T}_t^{\,A(\ln\tilde{T}_t)^2+B\ln\tilde{T}_t+C+D/\ln\tilde{T}_t}, \tag{2.25}$$

for constants A, B, C and D tabulated in table 2.1, where we have assumed the species to be in local equilibrium [10]. The quantity $\tilde{T}_t = T_t/[1\,\text{K}]$ has been introduced to ensure that the equation (2.25) is dimensionally consistent.

Table 2.1: Empirically derived constants for the collisional integral [10].

	N_2	O_2	NO	N	O	NO^+	e^-
A	0.114	0.0241	-0.2202	0	0.0164	0	0
B	-2.8945	-0.3467	5.2265	0	-0.2431	0	0
C	24.5080	1.3887	-40.5659	0	1.1231	-2.0000	-2.0000
D	-67.3691	-0.0110	104.7126	1.6094	-1.5561	23.8237	23.8237

As shown in equations (2.22) and (2.23), f_p and f_c can be determined when the species densities and the translational component of the temperature are known. In particular, using the species densities at thermal equilibrium and a pressure of 101.3 kPa presented in section 2.2.1, f_p and f_c are calculated and shown in figure 2.3b. Similar to figure 2.3a the values presented in figure 2.3b are not applicable to hypersonic missiles, but they can serve as a reference.

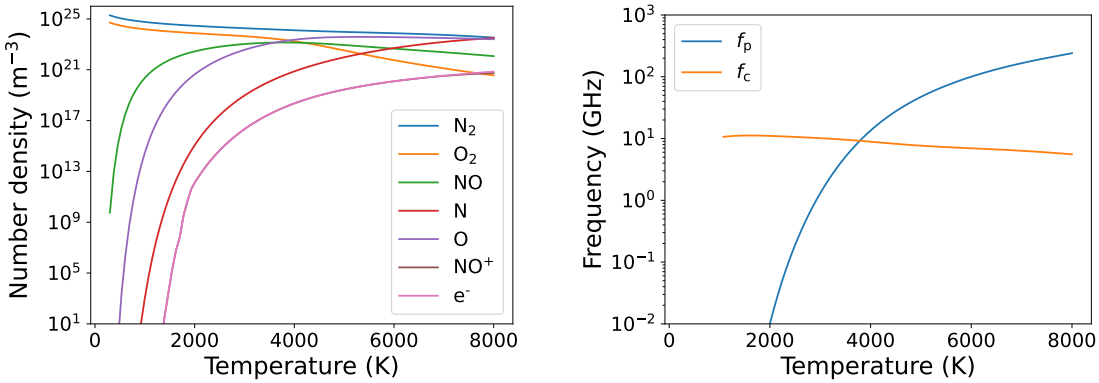

(a) (b)

Figure 2.3: Air initially composed of 21 % O_2 and 79 % N_2 at a pressure of 101.3 kPa heated isobarically. The chemical data is acquired from *Cantera*. In a), the number density of the chemical constituents is shown. Under the same thermal conditions, the plasma and collision frequencies are shown in b).

2.3 Wave propagation in plasmas

Under hypersonic conditions, the plasma sheath behaves as a conductive dielectric medium and is modeled using the Drude model [9]. The Drude model predicts that the relative complex permittivity of a plasma with plasma frequency f_p and collision frequency f_c is [9]

$$\hat{\varepsilon} = \frac{\varepsilon}{\varepsilon_0} = \varepsilon_\mathrm{real} + \mathrm{i}\varepsilon_\mathrm{imag} = 1 - \frac{f_\mathrm{p}^2}{f^2 + f_\mathrm{c}^2} - \mathrm{i}\frac{f_\mathrm{c}}{f}\frac{f_\mathrm{p}^2}{f^2 + f_\mathrm{c}^2}, \tag{2.26}$$

if it is exposed to an electric field with frequency f and has an ambient relative permittivity set to 1, which is an accurate approximation for ambient air. The real and imaginary components of the relative permittivity are denoted by $\varepsilon_\mathrm{real}$ and $\varepsilon_\mathrm{imag}$, respectively. The imaginary component of the permittivity can also be related to the conductivity σ_cond of the plasma by

$$\varepsilon_\mathrm{imag} = -\frac{\sigma_\mathrm{cond}}{2\pi f \varepsilon_0}. \tag{2.27}$$

Assuming that the plasma is exposed to a negligible magnetic field, then the complex index of refraction, $n = \sqrt{\hat{\varepsilon}}$, of the plasma can be written as

$$n = n_\mathrm{real} + \mathrm{i}n_\mathrm{imag} = \sqrt{\frac{|\epsilon_\mathrm{r}| + \epsilon_\mathrm{real}}{2}} + \mathrm{i}\sqrt{\frac{|\epsilon_\mathrm{r}| - \epsilon_\mathrm{real}}{2}}, \tag{2.28}$$

for the real and imaginary parts n_real and n_imag. Using equations (2.26) and (2.28) the index of refraction for small and large electric field frequencies can be shown to be

$$\lim_{f\to 0} n = \infty \tag{2.29}$$

$$\lim_{f\to \infty} n = 1. \tag{2.30}$$

From this, it can be concluded that an electromagnetic wave with low frequency f, incident on the interface of a long and homogeneous plasma with a high plasma frequency f_p, will be fully reflected. In contrast, for an electromagnetic wave with a frequency much higher than the plasma frequency, the plasma appears transparent. In the intermediate range, where f is comparable to f_p or f_c, the dynamics are complicated, especially when these vary spatially, as they do under realistic conditions.

In the case of a low-frequency wave that is totally reflected by the plasma, the underlying surface essentially becomes invisible to the wave. If that surface is rough, which implies that the surface backscatters strongly for waves at oblique incidence, the plasma can act as a shield and decrease the RCS.

2.4 1D model of wave reflectance

To simplify the scattering problem of an electromagnetic wave interacting with a missile surrounded by a spatially varying plasma and collision frequencies, a 1D model of the scattering is considered first.

Consider a plane wave propagating in air ($n_{\text{air}} = 1$) that impinges on a homogeneous plasma at normal incidence, with plasma frequency f_{p} and collision frequency f_{c}. The length of the plasma is l and it has a corresponding index of refraction n. The plasma covers a PEC slab. As the wave impinges upon the plasma, it gets partially reflected and partially transmitted. While the reflected wave continues to propagate endlessly without altering its form, the transmitted wave attenuates as it propagates through the plasma until it hits the PEC surface. There it is reflected and eventually all of the remaining wave is returned to the air, propagating in the opposite direction to the incident wave. A schematic of this setup is shown in figure 2.4.

The problem in this case is to determine the intensity of the reflected wave relative to the incident wave, $\rho = I_{\text{r}}/I_0$, and this has been solved analytically, with the solution [11]

$$\rho(f) = \frac{I_{\text{r}}(f)}{I_0(f)} = \left| \frac{(1-n)\text{e}^{-2\text{i}\varphi} - 1 - n}{(1+n)\text{e}^{-2\text{i}\varphi} - 1 + n} \right|^2 \tag{2.31}$$

$$\varphi = \frac{2\pi f n l}{c}, \tag{2.32}$$

where n is computed from equations (2.28) and (2.26). Notice that the 1D model described here has four free parameters: f, f_{p}, f_{c} and l. However, only three dimensionless quantities determine the solution, namely $f/f_{\text{p}}, f/f_{\text{c}}$ and $f \cdot l/c$. In figure 2.5, I_{r}/I_0 is plotted for a 3 GHz wave with corresponding wavelength 0.1 m at a few different plasma lengths. The figures can essentially be divided into three regions: I, II and III. In region I, $f_{\text{p}} \gtrsim f$ and the plasma is so dense that there is total reflection of the EM wave. While in region II, $f_{\text{p}} \sim f$ and significant attenuation occurs. Whereas in region III, $f_{\text{p}} \lesssim f$ and the plasma is so sparse that microwaves are essentially unaffected by the plasma. This behavior can be related to a damped harmonic oscillator composed of the free electrons, with a natural oscillation frequency f_{p}. Only driving frequencies f close to f_{p} induce motion in the electrons. For these frequencies, the electron motion is dissipated into heat due to the resistivity of this collisional plasma. Therefore, energy is lost for EM waves with frequencies close to f_{p}.

Furthermore, the domain size of the attenuated region grows with increasing plasma length, which is expected since a long plasma will have a longer interaction time with the EM waves compared to a shorter plasma. The local minima in figure 2.5 are caused by destructive interference between the EM wave reflected at the boundary of the plasma and the PEC behind the plasma. Neglecting these interferences, one can roughly say that the attenuation of the EM wave traveling from the plasma boundary to the PEC and back goes as $\text{e}^{-2n_{\text{im}}kl} = \text{e}^{-4\pi n_{\text{im}} f l/c}$, where k is the wavenumber. For significant attenuation, the length scale of this homogeneous plasma must be at least $l > c/4\pi f$. This is a consequence of the fact that n_{im} must be of order unity or smaller for EM waves entering the plasma, as large n_{im} lead to total reflection.

Figure 2.5 also indicates that the strongest attenuation can reach at least -30 dB. However, it is important to emphasize that this 1D model does not necessarily represent a realistic plasma generated by a hypersonic missile, even if the dimensionality

is taken into consideration. A realistic plasma has gradients, so the length scale of constant plasma and collision frequencies is considerably shorter than the entire plasma length. Moreover, as the attenuated frequencies depend on the plasma and collision frequencies, the overall attenuation at a particular microwave frequency is smaller than what is shown in figure 2.5.

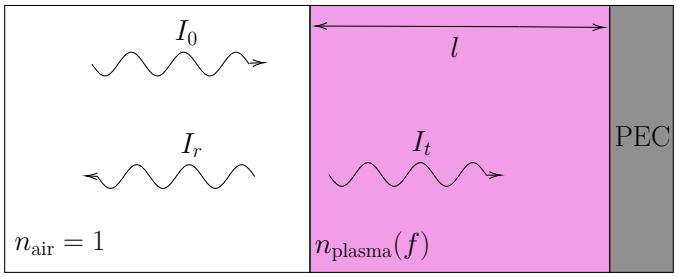

Figure 2.4: Schematic of a 1D model for the reflection of an electromagnetic wave at normal incidence against a homogeneous plasma with frequencies f_{p} and f_{c} and length l covering a metal. I_0, I_{r} and I_{t} are the intensities of the incident, reflected and transmitted waves, respectively.

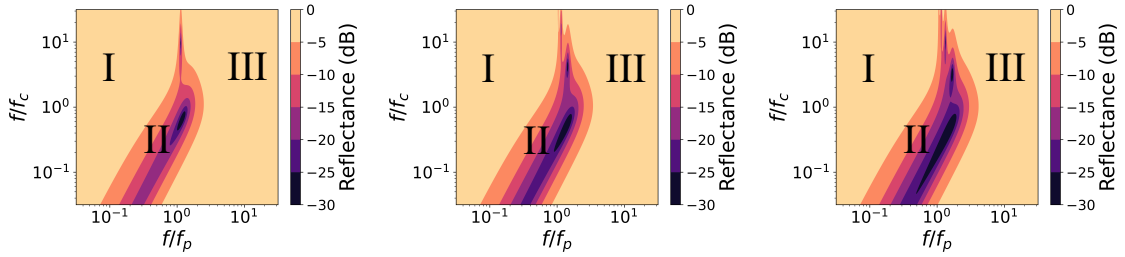

(a) (b) (c)

Figure 2.5: Reflectance, I_{r}/I_0, computed from equation (2.31) at different plasma frequencies, f_{p}, and collision frequencies, f_{c}. The microwave frequency is $f = 3\,\text{GHz}$. The plasma lengths are $l = 10\,\text{cm}$, $20\,\text{cm}$, $30\,\text{cm}$ in a), b) and c), respectively. The plotted parameter domains are divided into three regions: I, II and III, based upon the attenuation strength.

3

Simulations

For modeling the scattering of microwaves against plasma sheaths of hypersonic objects, two numerical tools have been used. The CFD solver *hy2Foam* for hypersonic flows [12] was used to compute the spatially varying plasma and collision frequencies. While the FDTD solver *meep* [20] was used to evaluate the scattered EM field of radar targets. The fundamental reason why the simulations can be split up in this manner is due to the short timescale of the microwave propagation in comparison to the plasma dynamics. Therefore, the plasma can be assumed to be static during an electromagnetic simulation. In this chapter, these two solvers will be described along with how they were applied in three of the four scenarios considered in this project. These scenarios were the EM scattering of a plasma-covered planar PEC surface, a plasma-covered rough PEC surface and a hypersonic PEC sphere. The remaining scenario was a completely analytical description of pulse compression for a plasma-covered planar PEC surface.

3.1 Hypersonic CFD tool *hy2Foam* for plasma distribution of hypersonic sphere

The two-temperature CFD solver *hy2Foam* is developed within the OpenFOAM framework [12]. In the CFD solver, the energy, momentum and mass equations are solved in parallel using a finite volume method. One of *hy2Foam*'s main features is to handle non-equilibrium thermodynamics by including Park's two-temperature model, which accounts for a single vibrational and electronic energy pool [13], a requirement for hypersonic flows. One temperature characterizes the molecular translational and rotational energies, while the other characterizes molecular vibrational and electron translational energies. The chemical data for the seven different species and their reactions, discussed in section 2.2.1, were taken from [14], with collision data provided by [10].

The transport models of Blottner and Eucken were used to model the shear viscosity and thermal conductivity [15, 16]. Diffusion was modeled by Fick's law, while the mixing rules were based upon the work by Armaly and Sutton [17, 18]. The turbulence was modeled using the $k-\omega$ shear stress transport model for the turbulent

kinetic energy k and the specific dissipation rate ω[1]. The spatial discretization is first-order accurate. For the time propagation, a first-order backward Euler method was used.

The geometries considered in this project were spheres, due to their rotational symmetry and the existence of an analytical solution of the Mie scattering for spheres in a vacuum. In particular, a sphere with a radius of 0.5 m was used. For simulating the flow around a sphere, the axisymmetric mesh shown in figure 3.1 was built with the *gmsh* tool [19]. It consists of 26500 elements and has dimensions of 1.6 m × 1.75 m for the base and height, respectively. The mesh spans 5° around the axis of symmetry, but since there is only one layer of elements, the geometry is effectively 2D. The upper and lower surfaces have Neumann boundary conditions, while the inlet on the left surface has fixed boundary values consistent with the ambient pressure, temperature, species concentrations and the relative velocity of the atmosphere at the considered altitudes. The field was also initialized with these values. Since only N_2 and O_2 were considered, their molar ratios were set to 79 % and 21 %, respectively. The surface temperature of the sphere was set constant at the ambient temperature of 293 K. Non-catalytic walls with no-slip boundary conditions were also applied at the sphere's boundary. The simulations were run for 10 ms, such that the flow field had converged, with time steps fulfilling the Courant condition. The Courant condition states that the timestep must satisfy $\Delta t < C_{\max}\Delta x/v$ in order for convergence for certain partial differential equations. Here $C_{\max} \sim 1$, Δx is the minimum spatial resolution and v is the maximum velocity.

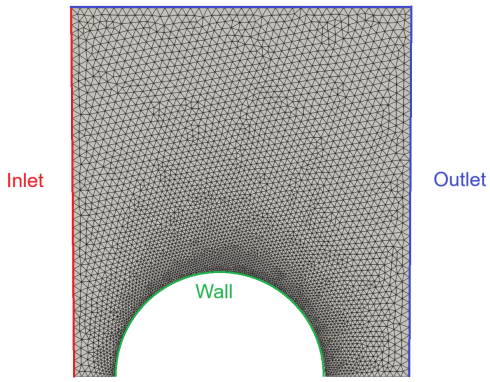

Figure 3.1: Axisymmetric mesh of sphere with radius 1.6 m. The dimensions are 1.6 m × 1.75 m for the base and height, respectively. The mesh spans up 5° around the axis of symmetry.

Once the field had converged, equations (2.22) and (2.23) were used to compute the plasma and collision frequencies. Since most of the plasma is generated in the stagnation region, where the pressure and temperature are highest, the mesh should

[1]Only in this context do k and ω refer to the turbulent kinetic energy and dissipation rate. Elsewhere in the report, the symbols represent the wavenumber and angular frequency.

ideally be sufficiently refined to capture the plasma gradients in that area. As it was later found, the mesh described above is believed to have been too coarse to resolve the stagnation region.

3.2 Electromagnetic FDTD tool *meep*

The FDTD solver for Maxwell's equations *meep* was used for the electromagnetic modeling of three out of the four scenarios considered in this project [20]. FDTD uses a staggered finite difference scheme in time and space to achieve second-order accuracy. In this project, FDTD is necessary, as the otherwise computationally efficient shooting and bouncing rays (SBR) method is not applicable to dispersive media such as a plasma. In order for FDTD to accurately propagate waves, the resolution of the grid must be significantly smaller than the shortest wavelength of the waves.

The plasma in *meep* was modeled as a Drude material satisfying equation (2.26), while the surfaces of the radar targets were assigned a permittivity of $\varepsilon = -\infty$ in order to scatter like a PEC. For the boundary, perfectly matched layers (PML) were added, with thickness $\lambda_{\max}/2$, where $\lambda_{\max}$ is the longest wavelength of the injected EM pulse. The purpose of the PML is to absorb EM waves without reflection in order to effectively simulate an infinite space. The mesh in *meep* was separate from the one used in the CFD simulations. In some electromagnetic simulations, artificial plasma and collision frequencies were used. In those cases, their use will be clearly stated. In the other simulations, the plasma and collision frequencies computed from the CFD simulations were interpolated onto the electromagnetic grid used in *meep* to create a plasma with reasonable spatial distribution.

In three of the four different scenarios, the scattered field was determined by injecting Gaussian pulses at the target. The pulses were modeled as plane waves, since the target of radar pulses can be assumed to be sufficiently far away from the emitting antenna compared to the wavelengths used. In all cases, a non-interacting *monitor* was placed around the PEC geometry and plasma to measure the electric and magnetic field components. This was done twice, once without the target to calibrate the monitor with the incident field and once with the target. The calibration removed the incident electric field $\mathbf{E}_{\text{inc}}$ from the total electric field $\mathbf{E}_{\text{total}} = \mathbf{E}_{\text{inc}} + \mathbf{E}_{\text{scatt}}$ in the second simulation. In this way, the scattered electric field $\mathbf{E}_{\text{scatt}}$ was recovered. The magnetic field was also taken into account.

Using the accumulated electric and magnetic fields at the monitors, the field at any point outside the monitors can in principle be analytically derived using Green's functions, assuming the propagation occurs in an effective vacuum. This was done from an internal *meep* command and was used in to determine the far-field for a collection of points. These points traced out a sphere centered at the simulation box, with a radius approximately 1000 times larger than the length scale of the simulation box. This returned the far-field in frequency space. The far-field was then used to compute the Poynting vector, which essentially points radially outward and

is therefore equivalent to the intensity. The scenarios were run until the scattered field had entirely been absorbed by the PML, with time steps satisfying the Courant condition.

3.2.1 Validation of *meep* for the 1D model

To validate the EM field solver in *meep*, the 1D model for the wave propagation in plasmas, discussed in section 2.4, was emulated in *meep*. The analytical solution was then compared to the simulation. A simulation was performed in which a Gaussian-pulse plane wave with intensity I_0 was injected into air. The pulse was polarized in the y-direction. The EM wave struck a homogeneous plasma at normal incidence. The plasma, with constant plasma and collision frequencies, covered a PEC. The simulation was 2D and the geometry was quasi-1D. The reflected wave coming out of the plasma had intensity I_r. The simulation box is shown in figure 3.2. The air is colored black, the plasma is white, the PEC is grey and the PML is hashed green lines. The red antenna is the source. The monitors colored in blue accumulated the intensity over the simulation as a spectrum.

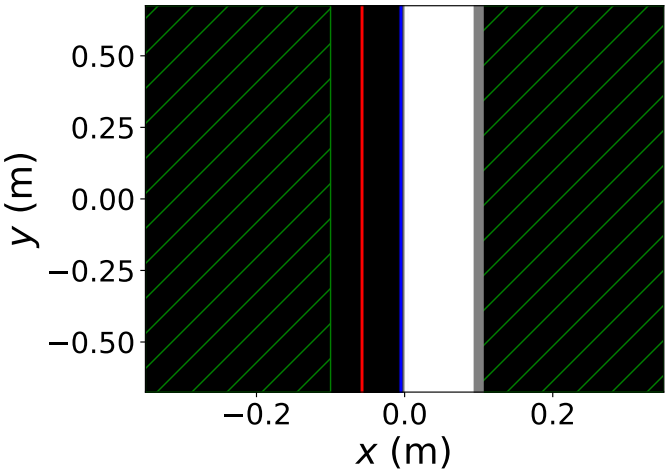

Figure 3.2: Simulation of the EM scattering from an effectively 1D homogeneous plasma struck by a Gaussian-pulse plane wave at normal incidence. The figure shows the simulation box. The PML is marked with green hashes, the air is black, the plasma is white, the PEC is grey, the source of the plane wave is red and the intensity monitor is blue.

The boundary conditions on the upper and lower sides were Bloch-periodic, meaning that for example the electric field $\mathbf{E}(y)$ satisfies $\mathbf{E}(y+H) = \mathbf{E}(y)e^{ik_yH}$ at the boundaries. The same condition applies to the magnetic field. The simulation was run for two cases. First, without the plasma and PEC, to determine the incident intensity $I_0(f)$. Second, it was run with the plasma and PEC present in order to determine the scattered intensity $I_\mathrm{r}(f)$. Due to the quasi-1D geometry of this setup, the fields only vary in the x-direction. For this reason, the far-field is equivalent to the near-field and the intensity of the scattered wave can be directly computed at the location of the monitor.

3.2.2 Scattering of plasma-covered rough surface

Rough surfaces are considered good scatters and have a large RCS for obliquely incident waves. In contrast, flat surfaces of infinite length theoretically backscatter no radiation at oblique angles. To study the ability of a plasma sheath to shield rough surfaces, which without plasmas are good scatterers, simulations were run in *meep*. A 2D setup was considered, containing a plasma-covered surface with a certain roughness. Similar to the previous scenario, described in section 3.2.1, a homogeneous plasma with constant plasma and collision frequencies was considered, covering a PEC slab. However, the difference between this setup and the one described earlier is the introduction of PEC bins with random height $h(y)$ and a constant width of 5 mm. These bins represent a surface roughness of the metal. The simulation box, with exaggerated bin heights, is shown in figure 3.3. The heights of the bins were sampled from a correlated multivariate normal distribution $h \sim \mathcal{N}(1\,\mathrm{cm}, e^{|y_i - y_j|/\delta} \cdot 0.25\,\mathrm{cm}^2)$, where i and j are indices of the positions and δ is a correlation strength parameter set to 1 cm. In the case of negative h, the absolute value of the samples was taken. The purpose of this distribution was to provide a simple, not necessarily accurate, representation of surface roughnesses of real-world objects, where the length scale of the roughness is much smaller than the wavelength. As in the previous scenario, a linearly polarized Gaussian-pulse plane wave was injected toward the slab, but unlike in the previous simulations, the waves were injected at oblique incidence. The same Bloch-periodic boundary condition was used in these simulations as in previous simulations.

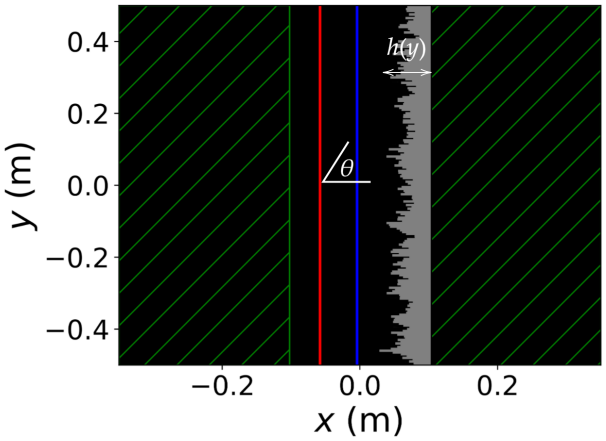

Figure 3.3: Simulation of the EM scattering from a 2D plasma with a Gaussian-pulse plane wave at oblique incidence angle θ. The figure shows the simulation box. The PML is hashed with green lines, the air is black, the PEC is grey, the source of the plane wave is red and the intensity monitor is blue. For clarity, the plasma is absent in this figure and the bin heights are exaggerated.

The intensities of the scattered and incident waves were accumulated by the monitors over the entire simulation and stored as a spectrum. As in the previous scenario,

the simulation was run twice. First, without the plasma and PEC and thereafter with them. From the accumulated scattered field at the monitors, the far-field was computed. Unlike in the previous scenario, the far-field is not equivalent to the near-field. The simulation was performed ten times, with different random seeds to average out the random distribution of the bin heights. The far-field from the ten simulations was summed up at the end.

3.2.3 Pulse compression for a plasma-covered surface

To investigate whether the mismatch loss, L_{MM}, which originates from the shape difference between the emitted and received signals, is significant for pulse compression, the 1D model from section 2.4 was used again. Using equation (2.31) for the reflectance, L_{MM} was determined analytically, without any simulations in *meep*.

Specifically, a broadband LFM pulse was assumed to be emitted from an antenna with carrier frequency f_{carr}, bandwidth B and pulse width T. Under ideal conditions, the emitted signal $s(t)$ should be proportional to the expression in equation (2.7). A PEC slab target was assumed to be at a distance R. For the reflection from a PEC slab with no plasma, the signal strength, $r_{\text{no plasma}}(t)$, is proportional to $s(t-R/2c)$. However, for a plasma-covered PEC slab, the reflected signal strength, $r_{\mathrm{plasma}}(t)$, is proportional to

$$\mathcal{F}^{-1}\left(\sqrt{\rho}\mathcal{F}\left\{s(t-R/2c)\right\}\right)(t), \tag{3.1}$$

where ρ is computed from equation (2.31) and $\mathcal{F}$ denotes the Fourier transform. The pulse-compressed signal was then computed by correlating the emitted signal with the reflected signal, similarly to section 2.1.2, as

$$y_{\text{no plasma}}(t) = \langle s(\tau), r_{\text{no plasma}}(\tau)\rangle\,(t) \tag{3.2}$$

$$y_{\mathrm{plasma}}(t) = \langle s(\tau), r_{\mathrm{plasma}}(\tau)\rangle\,(t), \tag{3.3}$$

omitting the uninteresting proportionality constants. Lastly, the mismatch loss, L_{MM}, was computed according to equation (2.10).

3.2.4 RCS and BRCS of hypersonic sphere

In sections 3.2.1, 3.2.2 and 3.2.3, artificial plasmas were considered. To study the effects of a realistic plasma on the RCS and BRCS, the spatial distribution of the plasma and collision frequencies obtained from the CFD tool were utilized. Simulations were run for a PEC sphere with a radius of 0.5 m. The sphere was coated with a plasma obtained using the method discussed in section 3.1. The simulation box is shown in figure 3.4. Surrounding the sphere and the plasma is a blue monitor that accumulates the intensity over the duration of the simulation. The region outside the monitor is assigned vacuum permittivity $\hat{\varepsilon} = 1$, effectively approximating the plasma and collision frequencies to 0. This approximation was not deemed significant for determining the RCS and BRCS, as the plasma in the region outside the monitor has been shown [21] to be mostly located behind the sphere and thus not important for the $\theta = 0$ aspect angle considered here. The reason for simulating

the wave propagation outside the monitor is twofold. First, to include a PML that absorbs the scattered waves as they approach the box boundary. Second, to provide some space between the PML region and the monitors.

A Gaussian-pulse plane wave, polarized in the y-direction, was injected in the direction parallel to the axis of the sphere. The simulation was run for two cases. First, without the sphere and plasma, to determine the incident field and then with the plasma and sphere to determine the scattered field. The far-field was then computed at points very far away from the sphere, similar to the description in section 3.2.2. The RCS and BRCS were computed according to equations (2.2) and (2.3). Notice that due to the direction of the incident wave, the RCS and BRCS were only computed for $\alpha = 0$ in equations (2.2) and (2.3).

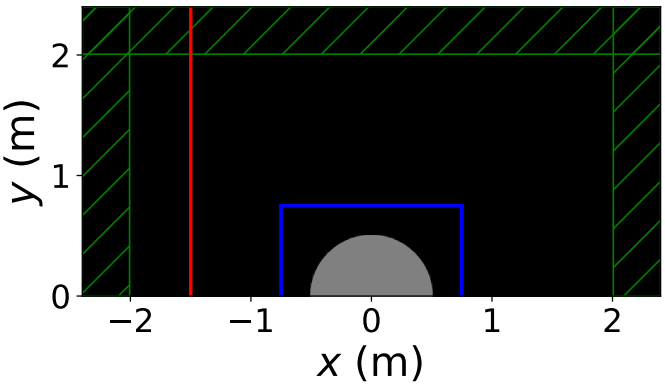

Figure 3.4: Simulation of the scattering of a plasma-covered sphere struck by a Gaussian-pulse plane wave. The figure shows the simulation box. The PML is marked with green hashes, the air is black, the PEC is grey, the source of the plane wave is red and the intensity monitor is blue. The plasma is absent in this figure. The geometry shown uses cylindrical coordinates, where y is analogous to r and x is analogous to z.

4

Results and discussion

In this chapter, the results will be presented in two sections. One section presents the CFD simulations of a sphere moving at different speeds, along with the corresponding distributions of plasma and collision frequencies. The other section presents electromagnetic scattering simulations using both a completely artificial plasma and a more realistic plasma that uses the plasma and collision frequency distributions from the CFD simulations.

4.1 Plasma distribution of hypersonic sphere

In order to predict the scattering of plasma-covered objects, it is of fundamental importance to have realistic plasma and collision frequency profiles. In this section, CFD simulations for a hypersonic sphere with speeds of $3\,\mathrm{km\,s^{-1}}$, $4\,\mathrm{km\,s^{-1}}$ and $5\,\mathrm{km\,s^{-1}}$ will be presented, along with their plasma and collision frequency profiles.

Axisymmetric CFD simulations were run for a sphere with a radius of 0.5 m at an altitude of 40 km, corresponding to an atmospheric pressure of roughly 290 Pa, moving at speeds of $3\,\mathrm{km\,s^{-1}}$, $4\,\mathrm{km\,s^{-1}}$ and $5\,\mathrm{km\,s^{-1}}$. A speed of $2\,\mathrm{km\,s^{-1}}$ was also tested, but it is not presented here as no plasma was generated. It is possible that a thin plasma could form at $2\,\mathrm{km\,s^{-1}}$ if the resolution was higher, but such a thin plasma would have negligible effects on the radar pulse. The sphere and ambient air were assumed to have a constant temperature of 293 K. In figure 4.1, the final results are plotted after the transient behavior has decayed. The first, second and third columns show the three different velocity scenarios in increasing order, while the rows show the plasma frequency, collision frequency and translational temperature, respectively.

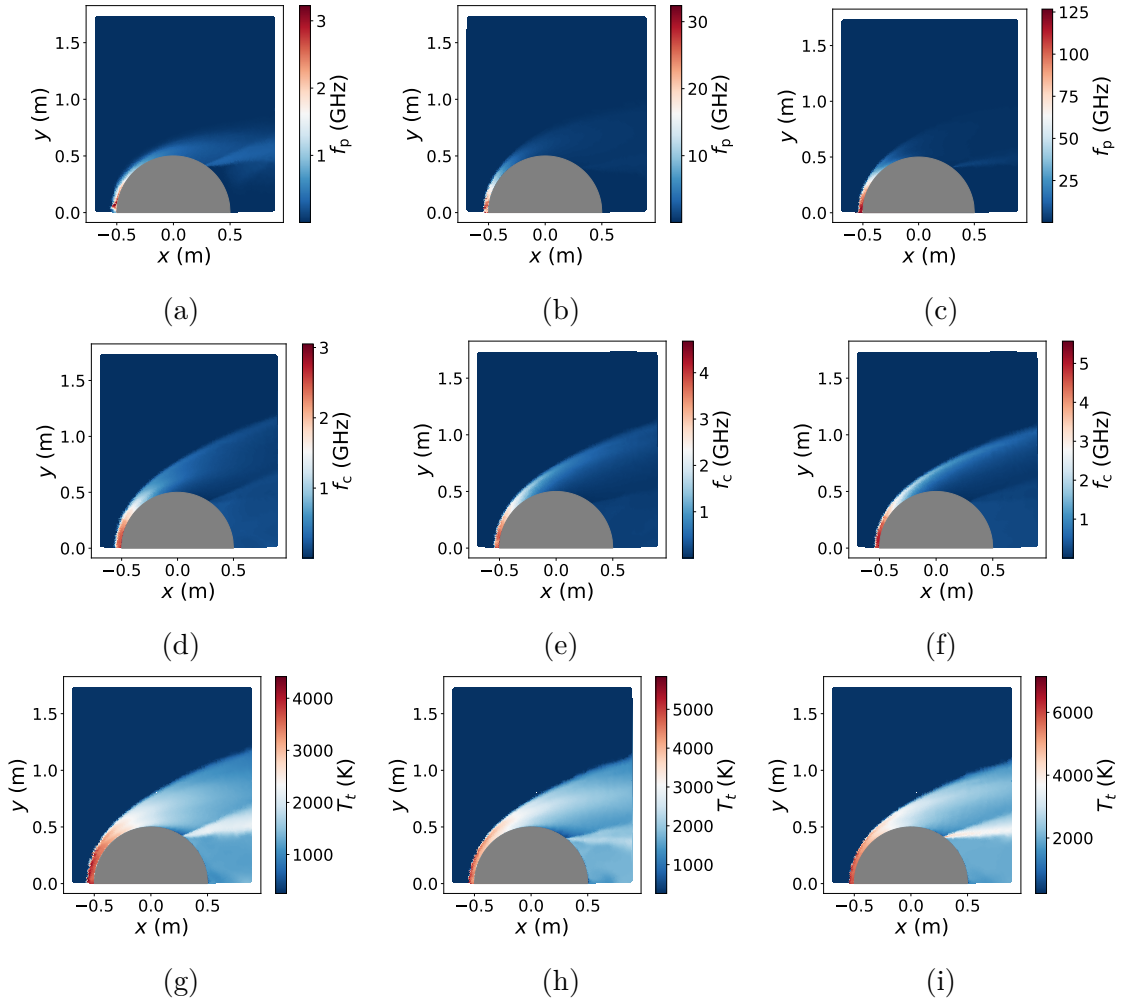

Figure 4.1: CFD simulations of a sphere moving at speeds of $3\,\mathrm{km\,s^{-1}}$, $4\,\mathrm{km\,s^{-1}}$ and $5\,\mathrm{km\,s^{-1}}$. The columns show the three velocity scenarios in increasing order, while the rows show the plasma frequency, collision frequency and translational temperature, respectively. The grey half-sphere indicates the cross-section of the sphere in this axisymmetric geometry.

The magnitudes of the plasma and collision frequencies at $4\,\mathrm{km\,s^{-1}}$ are reasonable compared to a similar study [21] done under similar conditions. The qualitative parabolic shape of the plasma and collision frequencies near the sphere also agree with [21]. Additionally, the three quantities f_p, f_c and T_t increase with speed, as expected. Moreover, f_p is much more sensitive to the speed than f_c, which aligns with figure 2.3b, showing a similar trend for temperature. This is not surprising, since f_c is roughly proportional to the density of molecules, while f_p scales as the root of the ionization degree, which depends exponentially on temperature. These observations indicate that the obtained frequencies are reasonable.

A large source of uncertainty is believed to originate from the mesh resolution, since the plasma is the most dense in the stagnation region. This region has large gradients and ideally needs to be well resolved. The lack of satisfactory resolution is believed to have caused the bump in the plasma frequency in figures 4.1a and 4.1b.

The temperatures in the stagnation region shown in figures 4.1g, 4.1h and 4.1i appear to be overestimated by about 1000 K when compared to a study by [2], which estimated the stagnation temperature at the nose of a hypersonic vehicle consisting of zirconium diboride. This temperature difference is substantial, which suggests that to more accurately predict the temperature around a hypersonic body, the heat flow between the body and air must be accurately accounted for. Furthermore, it highlights an unphysical setting used in the CFD simulations, namely that the temperature of the sphere was held at ambient temperature, 293 K. In summary, the plasma and collision frequencies appear reasonable, but they are probably not an accurate prediction of reality, as they are likely overestimated.

However, assuming that these plasma and collision frequencies are representative of missiles traveling at similar speeds, it can be concluded that radar systems using microwaves with frequencies slightly above the maximum plasma and collision frequencies shown in figure 4.1 are expected to be unaffected by the plasma. This is a consequence of the relative permittivity in equation (2.26) rapidly approaching 1 as f is increased above f_p and f_c, at which point the plasma becomes transparent to microwaves. Conversely, microwaves with frequencies below the maximum plasma frequency and collision frequency may either be totally reflected or partially attenuated.

In section 2.4, for the 1D model, it was stated that in order for a homogeneous plasma to significantly decrease the reflected signal, the condition $l > c/4\pi f$ must be satisfied. In the cases shown in figure 4.1, the length scale of the plasma regions with similar frequency is at most 10 cm. This implies $f > c/4\pi l \approx 240\,\mathrm{MHz}$, corresponding to a wavelength of roughly 1 m, which happens to be equal to the sphere's diameter in this case. Since radar systems often operate at frequencies above 240 MHz, this suggests that the plasma can potentially well affect the microwaves used by radars.

4.2 Electromagnetic scattering

The scattering of electromagnetic waves from a few plasma-covered objects is presented in this section. Two of these are 1D slabs with an artificial homogeneous plasma covering a PEC surface, both with and without surface roughness. The smooth PEC surface is used as a validation case to verify that *meep* models the plasma correctly. The other objects are plasma-covered spheres with realistic plasma and collision frequency profiles, as described in section 4.1.

4.2.1 Validation of *meep* for 1D model

In this section, a simulation based on the model discussed in section 2.4, involving the wave propagation in a homogeneous plasma covering a PEC surface, is used as a validation case for *meep*.

The intensity of the incident Gaussian wave, normalized to its peak value, is plotted

in figure 4.2a together with the reflected wave, normalized using the same factor. This was done for a case where the Gaussian source had central frequency $f_{\text{cen}} = 3\,\text{GHz}$ and $-3\,\text{dB}$-bandwidth equal to 1.2 GHz. The plasma and collision frequencies were set to 2.4 GHz and 150 MHz, respectively, and plasma length was 10 cm. The ratio of the reflected intensity $I_{\text{r}}(f)$ to the incident intensity $I_0(f)$ is plotted in figure 4.2b. The equivalent ratio predicted by equation (2.31) is also shown in figure 4.2b. The parameters were chosen to cause significant attenuation in order to check if *meep* and equation (2.31) predict similar ratios.

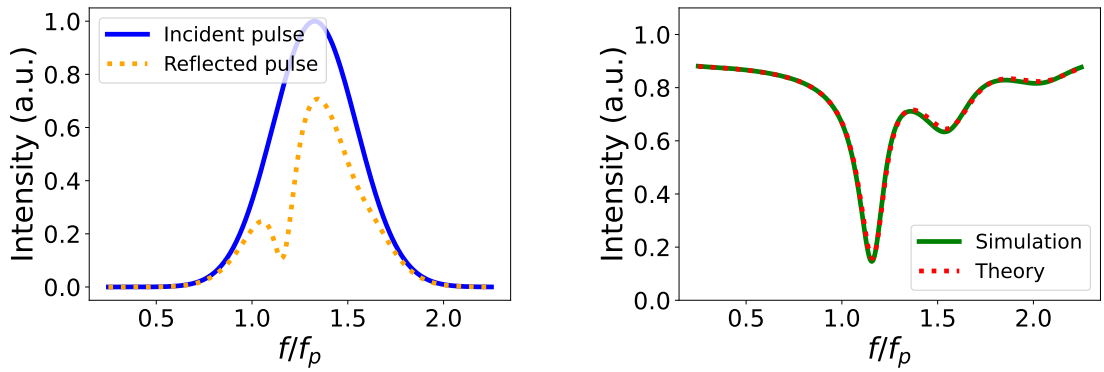

(a) (b)

Figure 4.2: Simulation of the scattering of a Gaussian-pulse plane wave impinging on a homogeneous plasma at normal incidence. In a), the normalized intensity spectrum of the incident pulse and reflected pulse is shown. In b), the spectrum of the reflectance is shown.

Figure 4.2a shows that the reflected pulse is distorted, that is, it does not have the same shape as the incident pulse. This is more clear in figure 4.2b, where the attenuation is the highest close to $f/f_p \approx 1$, which was also discussed in section 2.4. The figure also shows oscillations caused by resonances when the length of the plasma closely matches integer multiples of the microwave wavelength, as explained in section 2.4. Most importantly, the figure shows that *meep* can accurately model microwave absorption in the plasma, because theory and simulation agree.

4.2.2 Scattering of plasma-covered rough surface

In this section, results are presented for the scattering from a plasma-covered rough surface. A Gaussian-pulse plane wave with central frequency $f_{\text{cen}} = 3\,\text{GHz}$ and $-3\,\text{dB}$-bandwidth equal to 1.2 GHz was injected. The wave was sent at oblique angles towards the plasma-covered PEC surface. The plasma was uniformly distributed with a plasma frequency of $f_{\text{p}} = 2.4\,\text{GHz}$ and a collision frequency of $f_{\text{c}} = 150\,\text{MHz}$. The plasma length was 10 cm. As described in section 3.2.2, the surface consists of many thin bins to emulate a rough surface. The incident wave intensities are plotted in figure 4.3, where the angle θ is defined as the counterclockwise angle in the xy-plane with respect to the x-axis, shown in figure 3.3. The intensities are normalized to the peak value of the normal-incidence, $\theta = 0$, wave. The incident

angles were $\theta = \{0°, 20°, 40°, 60°, 70°\}$. Due to the finite size of the simulation box, the incident waves were not perfect plane waves, as the intensities have an angular width. The backscattered intensity is plotted in figure 4.4 at the different incidence angles, both with the bins and plasma present as well as absent. Figures 4.4a, 4.4b and 4.4c correspond to frequencies $f = 1.7\,\text{GHz}, 2.9\,\text{GHz}, 4.3\,\text{GHz}$, respectively, or equivalently $f/f_\text{p} = 0.7, 1.2, 1.8$. Notice that the angles in these figures are flipped 180° relative to figure 4.3. The scattered intensities are normalized such that the peak value for each corresponding incident wave is 1. This reflectance is proportional to the measured RCS. Similarly, figure 4.5 shows the scattered intensity for non-backscattered directions at the same frequencies, but only for the incident angle $\theta = 40°$. It is normalized in the same way as the figure 4.4. The scattered intensity is proportional to the measured BRCS.

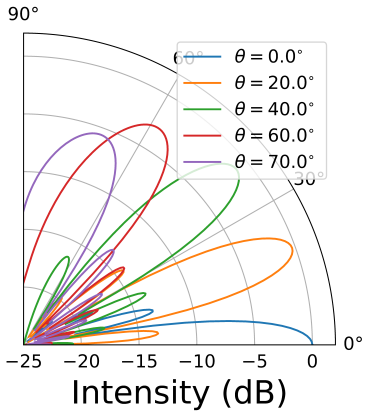

Figure 4.3: Incident wave intensities at frequency $f = 1.7\,\text{GHz}$ for five waves injected at oblique angles.

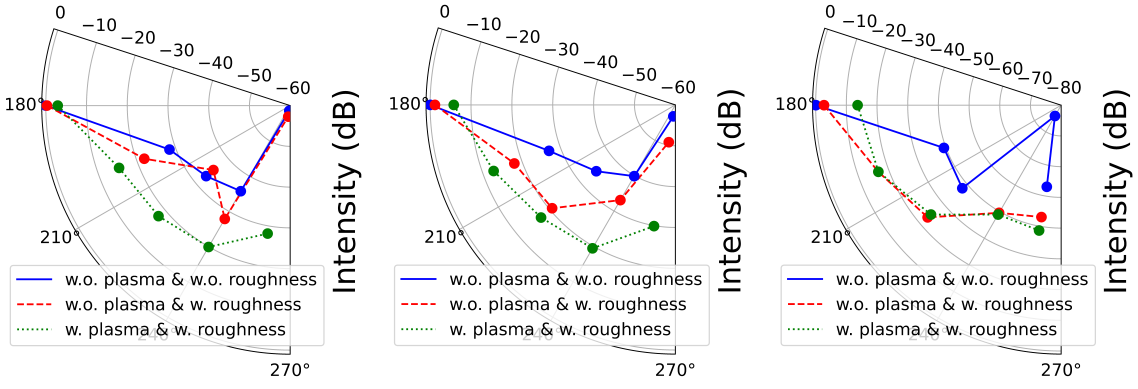

(a) (b) (c)

Figure 4.4: Backscattered intensities of a PEC slab at frequencies $f = 1.7\,\text{GHz}, 2.9\,\text{GHz}, 4.3\,\text{GHz}$ for figures 4.4a, 4.4b and 4.4c, respectively, for five different angles. Simulations were performed with the PEC bins and plasma present as well as absent.

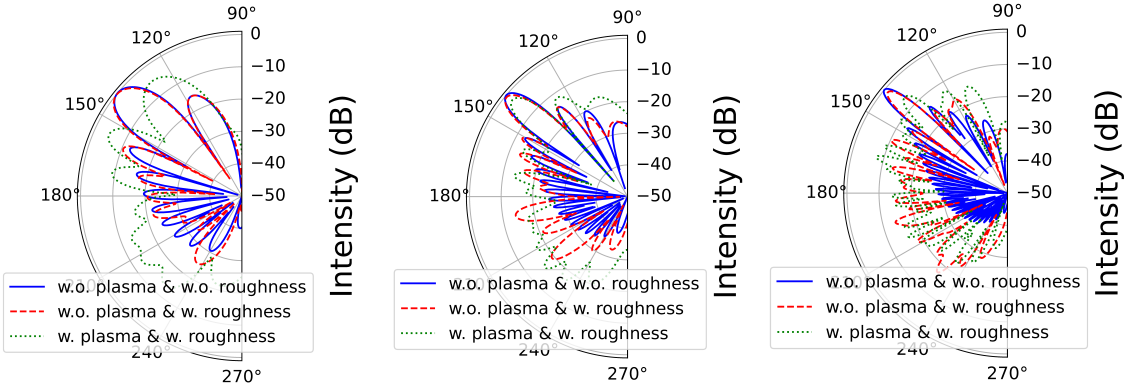

(a) (b) (c)

Figure 4.5: Scattered intensities of a PEC slab at frequencies $f = 1.7\,\text{GHz}, 2.9\,\text{GHz}, 4.3\,\text{GHz}$ for figures 4.5a, 4.5b and 4.5c, respectively, where the incident angle was $\theta = 40°$. Simulations were performed with the PEC bins and plasma present as well as absent.

Adding surface roughness in the form of PEC bins on top of the flat PEC surface should spread the scattered radiation over wider angles compared to using a flat surface. This prediction agrees with the results presented in figures 4.4 and 4.5, no matter if the plasma is present or not. As a consequence, there is a slight decrease in the intensity of the scattered radiation at the reflection angle, which in the case of figure 2.3 is $180° - 40° = 140°$. However, this effect is barely visible because the bin heights are much shorter than the wavelengths of the microwave pulse. If shorter wavelengths were used, the modeled roughness would have directed more radiation into the non-reflection angles. How much the roughness scatters in absolute terms is not of interest for this project. The focus lies on the relative difference in scattering intensity between a rough surface with plasma present and one without a plasma. Therefore, features like the sidelobes in figure 4.5 for rough surfaces are not of interest in themselves. Although, the oscillations most likely stem from the constant bin width, as supported by the observation that the separation between them increases with frequency. In summary, the most important qualitative observation is that the results agree with the expectation that adding roughness to a flat PEC surface spreads out the radiation.

For the frequency dependence, we would expect the plasma to behave according to the three regions discussed in section 2.4. As the same plasma parameters were used in section 4.2.1, figure 4.2b acts like a useful reference point. For the three frequencies shown, we are roughly located in regions I, II and III. First, for the scattering in figures 4.4a and 4.5a, the plasma is expected to behave like a mirror, effectively shielding the rough surface. As a result, the scattered intensity with the plasma present is expected to more closely resemble that of a flat PEC surface than that of a rough surface. This expectation is contradicted by the observations in figure 4.4a, as the plasma enhances the scattering. The reason for this discrepancy is unclear and might be a sign of an error in the simulation code, a refraction effect in the plasma due to the oblique incidence, or that the simulation has not numerically

converged.

Second, for the scattering shown in figures 4.4b and 4.5b, the plasma is expected to attenuate the radiation. This attenuation factor should roughly be $-10\,\mathrm{dB}$, as predicted by figure 4.2b at the relevant frequency $f = 2.9\,\mathrm{GHz}$. However, this is not observed in figures 4.4b and 4.5b. Instead, adding plasma to the rough surface even increases the scattered intensity by more than 10 dB in the sidelobes. Third, for the scattering in figures 4.4c and 4.5c, we expect the plasma to be mostly transparent to the radiation. Therefore, the presence of the plasma should not significantly affect the scattering. This prediction mostly aligns with the results shown in figures 4.4c and 4.5c. Given that the scattered intensities behave unexpectedly and agree somewhat poorly with the predictions in Section 2.4, the results presented in figures 4.4 and 4.5 should be viewed with skepticism.

Assuming the results are accurate, adding plasma to the rough surface does not simply reduce the scattered intensities. Instead, it can either increase or decrease the scattered radiation depending on the frequency and angle. To illustrate this complex behavior, we can see in figure 4.5 that the intensity at the reflection angle is always lowest when plasma is present. Most of the scattering radiation is also concentrated in the direction of the reflection angle. The plasmas considered here are modeled as dielectrics and can only absorb or redirect radiation, not produce it. Therefore, the radiation at the reflection angle is always lower for a plasma-covered rough surface than for a rough surface without plasma. For realistic plasmas surrounding cone-like geometries, however, this may no longer be the case. In those scenarios, the plasma might be able to effectively increase the cross-sectional area, making more radiation scatter in the direction of the reflection angle. This contrasts with the geometry used here, which has the same cross-sectional area regardless of the presence of plasma.

Another indication of this complex behavior is the increased backscattered radiation in figure 4.4 when a plasma is added for some of the larger angles. Similarly, in figure 4.5, the scattered radiation increases at certain angles with the addition of plasma and decreases at others. One possible explanation for this is the sampling. It is possible that ten simulations were not sufficient to represent the whole space of bin heights needed to achieve the desired accuracy in the intensity results. However, this is probably not the main contributor to the increased scattering when adding plasma, as the plasma-covered rough surface shows intensities more than 10 dB higher than the rough surface without plasma, for some angles, at lower frequencies.

In summary, the presented results for the scattering from a plasma-covered rough surface may be unreliable. This is evident when comparing the attenuation for normal incidence predicted in figure 3.2 at the relevant frequencies with the simulated scattering intensities shown in figures 4.4. For oblique angles, there might still exist effects that need to be considered and investigated. To address the question regarding the numerical convergence of the results, an analysis varying the spatial resolution would be beneficial. If the results are to be trusted, adding plasma to a rough surface does not consistently decrease the scattered intensity across all angles

and frequencies. At some angles and frequencies, the scattering is enhanced by the plasma. The observations made in this section are difficult to extrapolate to more realistic plasmas with complex spatial distributions. Further study is needed to investigate the ability of plasma sheaths to shield rough surfaces.

4.2.3 Pulse compression for a plasma-covered surface

In this section, the results from an analytical approach for determining the mismatch loss, L_{MM}, are presented. A broadband LFM pulse was used, with carrier frequency $f_{\mathrm{carr}} = 3\,\mathrm{GHz}$, bandwidth $B = 300\,\mathrm{MHz}$ and pulse width $T = 3.3\,\mu\mathrm{s}$. The distance to the target PEC surface was set to $R = 1\,\mathrm{km}$. This distance is arbitrary, as it only translates the peak in the pulse compression. For the homogeneous plasma, the plasma and collision frequencies were set to $f_{\mathrm{p}} = 2.4\,\mathrm{GHz}$ and $f_{\mathrm{c}} = 300\,\mathrm{MHz}$, respectively. The plasma length was $l = 10\,\mathrm{cm}$.

In figure 4.6a, the spectra of the received signals are shown for a PEC surface with and without plasma. The intensity is normalized to the peak value of the pulse without plasma. Figure 4.6b shows the corresponding pulse-compression amplitude as a function of the detection range R, which is identical to $ct_0/2$, where t_0 is the flight time of the pulse. From the pulse compression, the mismatch loss was determined to be $L_{\mathrm{MM}} = 0.73 = -1.4\,\mathrm{dB}$. The plasma frequency, f_{p}, and collision frequency, f_{c}, were then varied while keeping l, f, B, T and R constant, allowing L_{MM} to be computed for each combination of f_{p} and f_{c}. Figure 4.6c shows the results from this parameter scan.

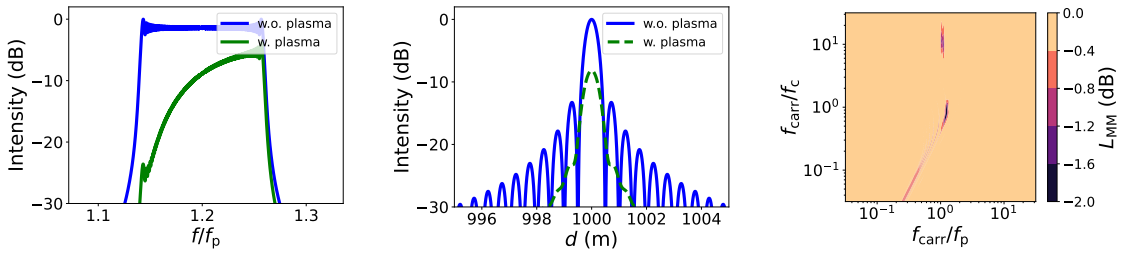

(a) (b) (c)

Figure 4.6: LFM pulse compression results for a plasma-covered PEC surface at constant plasma frequency and collision frequency. In a), the spectra of the received pulses for a PEC surface with and without the plasma are shown. In b), the corresponding pulse compression amplitude is shown. The difference in amplitude between the two peaks in b) is the mismatch loss, L_{MM}. In c), the L_{MM} for a parameter scan is shown.

Figure 4.6a shows that the attenuation is strongly frequency-dependent, i.e., the gradient of the intensity with respect to the frequency is high. This is not a new observation, as a similar pattern can be seen in figure 4.2b for a plasma with a different collision frequency. However, with regard to the mismatch loss, it suggests at the possibility of a significant L_{MM}. Still, $L_{\mathrm{MM}} = -1.4\,\mathrm{dB}$ is small compared to the energy loss, L_{E}. Figure 4.6b supports this view, as the shape of the pulse-

compressed signal for the plasma-covered slab is of similar shape to the slab with no plasma. The difference in peak amplitude can primarily be attributed to the energy loss in the plasma, i.e., $L_{\text{tot}} \approx L_{\text{E}} = -7.2\,\text{dB}$ by equation (2.10). Figure 4.6c supports the idea that L_{MM} is negligible for most plasma and collision frequencies.

The narrow frequency band in figure 4.6c is a consequence of the gradient of the reflectance with respect to the carrier frequency being high in figure 2.5. In this band, present in figure 4.6c, where L_{MM} reaches $-2\,\text{dB}$, is likely not even reachable for realistic plasmas. First, in realistic plasmas around shockwaves, the plasma and collision frequencies are not homogeneous but gradients. As a consequence, for a microwave pulse with a given carrier frequency, the II region described in section 2.4 is probably only attained in a spatial region with a length scale smaller than the full plasma length, which was set to 10 cm in this case. This would lead to a smaller attenuation and therefore a smaller L_{MM}. Second, the LFM pulse used in this analysis had a wide bandwidth of 300 MHz, which is necessary to produce significant mismatch between the emitted and received signals. This is because, as shown in figure 2.5a, the width of the II region in terms of f_{p} is typically on the order of the carrier frequency. Therefore, L_{MM} values in figure 4.6c likely overestimate the mismatch loss for systems with more modest bandwidths below 300 MHz. Nevertheless, radar systems using very wide bandwidths or, equivalently, those with high range resolution might be vulnerable to the distorting effects of plasma sheaths. Consequently, advanced techniques like high range resolution classification, which resolve individual components of targets, might be less effective for sufficiently quick hypersonic missiles.

For the reasons described above, we can safely assume that the distortion, described by L_{MM}, as described by the frequency-dependent attenuation of the plasma,, is negligible in most practical radar applications. However, the losses due to total energy absorption by the plasma, L_{E}, might still be significant.

4.2.4 RCS and BRCS of hypersonic sphere

In this section, results are presented for the RCS and BRCS of a hypersonic sphere moving at speeds of $3\,\text{km}\,\text{s}^{-1}$, $4\,\text{km}\,\text{s}^{-1}$ and $5\,\text{km}\,\text{s}^{-1}$ at an altitude of 40 km. The RCS and BRCS are shown for the case where a radar pulse propagates in the opposite direction to the sphere's motion. The spatial profile of the plasma is taken from the results presented in section 4.1.

A Gaussian-pulse plane wave with a central frequency of $f_{\text{cen}} = 1.9\,\text{GHz}$ and $-3\,\text{dB}$-bandwidth equal to 900 MHz was injected. From the scattered field, the normalized RCS, $\sigma_{\text{RCS}}/\pi r^2$, and the normalized BRCS, $\sigma_{\text{BRCS}}/\pi r^2$, were computed according to equations (2.2) and (2.3) for hypersonic spheres traveling at different speeds. The simulated RCS is shown in figure 4.7, along with the simulated RCS of a sphere without any plasma and the corresponding analytical result according to Mie theory, as described in section 2.1.3. Similarly, the simulated BRCS is shown in figure 4.8 alongside the analytical results for the case with speed $5\,\text{km}\,\text{s}^{-1}$ at frequencies 300 MHz, 600 MHz and 1.5 GHz.

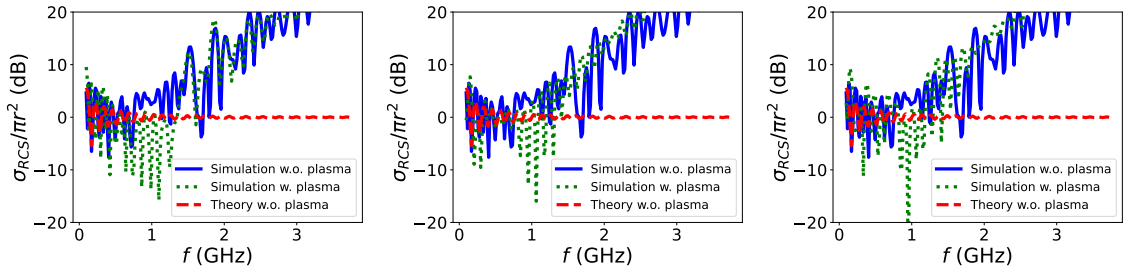

(a) (b) (c)

Figure 4.7: RCS of a hypersonic sphere moving at an altitude of 40 km and at speeds of 3 km s^{-1}, 4 km s^{-1} and 5 km s^{-1} is shown in figures 4.7a, 4.7b and 4.7c, respectively. The aspect angle is 0°, meaning that the incident wave propagates in the opposite direction to the motion of the sphere. The blue and red curves in each figure are identical.

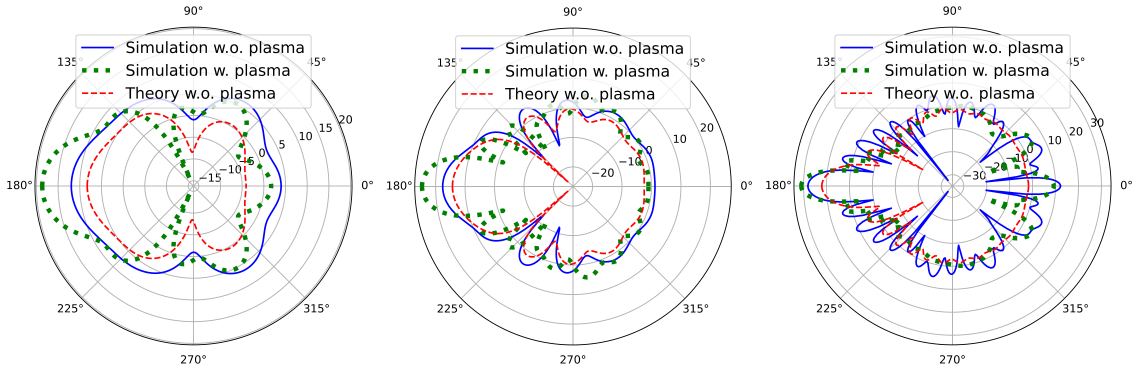

(a) (b) (c)

Figure 4.8: BRCS of a hypersonic sphere moving at an altitude of 40 km and at a speed of 5 km s^{-1}, at frequencies 300 MHz, 600 MHz and 1.5 GHz is shown in figures 4.7a, 4.7b and 4.7c, respectively. The aspect angle is 0°, meaning that the incident wave propagates in the opposite direction to the motion of the sphere.

The simulated RCS appears to be somewhat accurate for frequencies up to roughly 1 GHz. This is evident from figure 4.7, as the bare sphere has a RCS close to the result predicted by Mie theory up to this frequency. The BRCS in figure 4.8 behaves similarly. The accuracy worsens at higher frequencies, as the RCS is overestimated in figure 4.7. Likewise, the extinction angles, where the BRCS rapidly decreases, are accurate for figures 4.8a and 4.8b while inaccurate for the high frequency in figure 4.8c. This highlights a major disadvantage of FDTD simulations. In FDTD simulations, the grid resolution limits the smallest wavelength or largest frequencies that can be resolved. For this reason, in order to accurately predict the RCS at high frequencies, either the simulation box and the sphere must be decreased in size or significantly more computational power must be devoted to the simulations. The latter is inefficient, as the problem scales as $\sim \Delta x^{-3}$, where Δx is the grid length. This is because the simulations are 2D with time resolution proportional to

the grid resolution. Therefore, we are limited to analyzing low frequencies in FDTD simulations.

Although the simulated RCS and BRCS are inaccurate for high frequencies, the results show that at frequencies below roughly 1 GHz, the plasma can both increase or decrease the RCS and BRCS for the speeds considered here. The difference between the plasma-coated and bare sphere in figure 4.7 appears to be greatest for the $5\,\mathrm{km\,s^{-1}}$ case and smallest for the $3\,\mathrm{km\,s^{-1}}$, which aligns with intuition. However, the speed dependence does not seem strong and since the simulated RCS is slightly inaccurate even at low frequencies, it is difficult to determine whether the difference is due to physical or numerical effects.

A similar numerical study was performed on a weakly reflective sphere made of polytetrafluoroethylene, moving at a speed of $4\,\mathrm{km\,s^{-1}}$ and at an altitude of 40 km [21]. For our purposes, using a PEC sphere is more realistic than a sphere made out of polytetrafluoroethylene, also known as Teflon. In that study, it was found that the plasma sheath increased the RCS of the sphere by about 20 dB at 3 GHz. This effectively made the RCS of their plasma-coated and weakly reflective sphere similar to the RCS of an equivalent PEC sphere. Hence, the assumption of a PEC surface studied in this thesis is highly relevant when comparing the plasma-coated sphere to the bare sphere. Furthermore, it suggests that the plasma sheath around a sphere primarily acts as a total reflector if the plasma frequency is high enough. This is in agreement with the discussion in section 2.2, where it was concluded that for frequencies $f < f_\mathrm{p}$ the plasma behaves like a total reflector. Although, the important distinction here is that the plasma and collision frequencies have realistic spatial dependencies instead of being homogeneous.

However, one cannot simply say that the plasma acts like a total reflector for *all* frequencies fulfilling $f < f_\mathrm{p}$, if the results are accurate. In figures 4.1b and 4.1c, the plasma frequencies exceed 1 GHz, close to the sphere. As figures 4.7b and 4.7c indicate, when the microwave frequency is roughly 1 GHz, the RCS is attenuated by about -10 dB. Naively, we would expect the plasma sheath to not change the RCS at these frequencies or possibly increase it by a few dB, due to the cross-section of the plasma sheath being slightly larger than that of the bare sphere. Therefore, the plasma sheath's effect on the RCS cannot be explained solely by the maximum plasma frequency close to the sphere. For this reason, realistic plasmas with high plasma frequencies do not simply behave like total reflectors at all frequencies.

In summary, the simulated RCS and BRCS are only somewhat accurate at frequencies below 1 GHz and inaccurate for frequencies above 1 GHz. At these low frequencies below 1 GHz, the RCS and BRCS can both be increased and decreased by the presence of the plasma. Additionally, the assumption of a PEC surface for the sphere is of significant importance, as the plasma can increase the radar signature of a weakly reflective surface more than that for a PEC surface. Finally, it is difficult to interpret the nuances in the results, as the spatial distribution of the plasma and collision frequencies makes the scattering of EM waves complex and it is difficult to distinguish these effects from the numerical convergence issues.

5

Conclusions

In this thesis, the microwave scattering of plasma-covered geometries has been studied. The plasma was characterized by the plasma and collision frequencies and their spatial distributions. Three types of geometries were considered: a planar slab, a planar slab with surface roughness and a sphere. The slabs were coated with artificial homogeneous plasmas, while the sphere was coated with a realistic plasma consistent with the conditions present in the atmosphere for a spherical projectile traveling at hypersonic speeds.

Using an idealized 1D geometry with a homogeneous plasma, it was shown that the backscattered intensity can qualitatively be divided into three regions depending on the plasma length, microwave frequency, plasma and collision frequencies. In each region, the plasma either acted as a perfect mirror, attenuated the wave, or was transparent to the incident microwave. At normal incidence, it was concluded that significant attenuation occurs only when the microwave and plasma frequency are of similar magnitude.

To evaluate the effect of thin plasma at oblique incidence for a rough planar surface, roughness was added to a PEC slab and waves were injected at oblique incidence, which required the FDTD simulations to be performed in 2D. Assuming that the results from the simulations are accurate, adding a plasma to a rough surface does not simply reduce the scattered intensity at all angles and frequencies. At some angles and frequencies, the scattered intensity is enhanced. Since the scattered intensity is proportional to the BRCS and RCS at the backscattered angle, the results suggest that, in this idealized geometry, the radar signature for a rough surface is not necessarily decreased by the presence of a plasma. However, it remains unclear whether this conclusion holds for inhomogeneous plasmas and whether the simulations were accurate.

In order to address the question regarding the impact of the distortion induced by the plasma for pulse-compressed waveforms, an idealized geometry was again considered, consisting of a homogeneous plasma covering a PEC slab. Using analytical methods, microwaves at normal incidence were reflected from the surface. The spectrum of the returned signal was then correlated with the injected signal. The distortion was characterized by the mismatch loss due to the difference between the shapes of the two signals. A sweep was performed over a range of plasma and collision

frequencies, yielding a negligible mismatch in almost all cases. For realistic plasmas, it was concluded that the mismatch is negligible.

Naturally generated plasmas from hypersonic shock heating and the corresponding plasma and collision frequency spatial distributions were studied by performing CFD simulations for a sphere at an altitude of 40 km traveling at speeds of $3\,\mathrm{km\,s^{-1}}$, $4\,\mathrm{km\,s^{-1}}$ and $5\,\mathrm{km\,s^{-1}}$. The spatial dependence of these two frequencies was deemed qualitatively correct. In agreement with theory, the plasma frequency was sensitive to the speed, while the collision frequency was not. Quantitatively, the plasma and collision frequencies appeared reasonable at the considered altitude and speeds based on comparison with values reported in literature.

Using the spatial distributions of the plasma and collision frequencies from the CFD simulations, FDTD simulations were performed for a sphere with a radius of 0.5 m. By performing these simulations, the scattering amplitudes for monostatic and bistatic setups could be evaluated for a naturally generated plasma sheath around a metal sphere. For relatively low frequencies below 1 GHz, it was concluded that the RCS and BRCS at an aspect angle of $\theta = 0$ could either increase or decrease due to the presence of the plasma, depending on the exact microwave frequency. In some cases, the difference between a bare sphere and a plasma-coated sphere exceeded 10 dB. It has been observed that the RCS can increase significantly, by roughly 20 dB for weakly reflective surfaces [21], which is much more than what was found in this thesis for a PEC surface. Therefore, the assumption of a PEC surface was deemed important, as a PEC surface is less influenced by plasma than a weakly reflective surface is [21]. Finally, due to the complex spatial dependence of plasma and collision frequencies, it is difficult to explain the nuances of the scattering around a plasma-coated object.

5.1 Outlook

There are plenty of challenges within the study of plasma-induced stealth of hypersonic vehicles. One of the greatest is the lack of open data to validate the numerically predicted radar signatures against. Constructing an experiment to gather such data poses many practical and technical challenges. For this reason, the experimental research published by the German Fraunhofer research institute is a welcome addition to the field [3].

Another challenge, not as important as the lack of experimental data but still valuable for the design of robust radar, is the lack of a reference table relating the plasma frequency to a hypersonic vehicle's speed and altitude. This issue can be resolved relatively straightforwardly by performing a parameter sweep over the speed and altitude for a simple geometry. Such an approach would ultimately identify the speed and altitude ranges at which the plasma has a negligible effect on the radar signature. However, this method runs the risk of being too computationally expensive for sufficiently resolved meshes.

On a more fundamental level, it would be of interest to investigate the scattering of EM waves by plasma with perhaps a linear frequency dependence in a 1D or 2D scenario in order to further develop the theory presented in section 2.4. It might even be possible to construct an analytically solvable problem of this character.

Furthermore, improving upon the method used in this thesis to study plasma-coated rough surfaces is worth pursuing. The results shown on this topic were likely not very reliable and some were counterintuitive. Therefore, a more thorough analysis is needed. Moreover, it might be interesting to also explore details about the polarization of EM waves scattered from a plasma-coated rough surface.

Lastly, although it provides no extra scientific value, it may still be of interest for future studies to consider using multiphysics tools. Solving for the CFD and EM separately in two different environments, as was done in this thesis, was time-consuming and can potentially be streamlined in future work. Nevertheless, the packages used in this thesis have the advantage of being open-source and well-documented.

Bibliography

[1] Missile Defense Advocacy Alliance, "3M22 Zircon," 2025. [Online]. Available: https://missiledefenseadvocacy.org/missile-threat-and-proliferation/todays-missile-threat/russia/3m22-zircon/ (accessed on: 2025-04-16).

[2] M. Evestedt and K. Kraft, "On the Performance of Hypersonic Glide Vehicles," FOI, Stockholm, Sweden, FOI-R–5152–SE, 2021. [Online]. Available: https://foi.se/en/foi/reports/report-summary.html?reportNo=FOI-R–5152–SE, Accessed on: 2025-04-28.

[3] R. Petervari, S. Weidner, A. Nekris, S. Brüggenwirth, and P. Knott, "The Measurement of Radar Plasma Signatures in a Hypersonic Shock Tunnel: Simulation and Experiment," *IEEE Transactions on Aerospace and Electronic Systems*, vol. 59, no. 6, pp. 8581-8597, Dec. 2023, doi:10.1109/TAES.2023.3310497.

[4] Xu et al., "Evaluations of plasma stealth effectiveness based on the probability of radar detection," *IEEE Transactions on Plasma Science*, vol. 45, no. 6, pp. 938–944, Jun. 2017, doi:10.1109/TPS.2017.2700012.

[5] A. Hein, *Processing of SAR Data: Fundamentals, Signal Processing, Interferometry*. Heidelberg, Germany: Springer, 2004.

[6] C. Balanis, *Advanced Engineering Electromagnetics*. 2nd ed., Hoboken, NJ, USA: Wiley, 2012.

[7] J. Anderson, *Hypersonic and High temperature Gas Dynamics*. 2nd ed., Reston, VA, USA: AIAA, 2006.

[8] D. Goodwin, H. Moffat, I. Schoegl, R. Speth, and B. Weber, *Cantera: An object-oriented software toolkit for chemical kinetics, thermodynamics, and transport processes*. https://www.cantera.org, 2024. Version 3.1.0. doi:10.5281/zenodo.14455267.

[9] N. Ashcroft, and N. Mermin, *Solid State Physics*. Orlando, FL, USA: Harcourt, 1976.

[10] R. Gupta, J. Yos, R. Thompson, and K. Lee, "A Review of Reaction Rates and Thermodynamic and Transport Properties for an 11-Species Air Model for

Chemical and Thermal Calculations Roop N. Gupta Scientific Nonequilibrium to 30 000 K," NASA, Washington, DC, USA, RP-1232, 1990. [Online]. Available: https://ntrs.nasa.gov/citations/19900017748, Accessed on: 2025-04-16.

[11] L. Brekhovskikh, and O. Godin, *Acoustics of Layered Media I: Plane and Quasi-Plane Waves*. Heidelberg, Germany: Springer, 1990.

[12] V. Casseau, "An open-source CFD solver for planetary entry," Ph.D. dissertation, Department of Mechanical and Aerospace Engineering, University of Strathclyde, Glasgow, United Kingdom, 2017. [Online]. Available: 10.48730/fc4y-6m27

[13] C. Park, "The Limits of Two-Temperature Kinetic Model in Air," in *48th AIAA Aerospace Sciences Meeting Including the New Horizons Forum and Aerospace Exposition*, Orlando, FL, USA, 2010. [Online]. Available: doi:10.2514/6.2010-911, Accessed on: 2025-05-21.

[14] C. Park, "Review of Chemical-Kinetic Problems of Future NASA Missions, I: Earth Entries," *Journal of Thermophysics and Heat Transfer*, vol. 7, no. 3, pp. 385-398, Jul. 1993, doi:10.2514/3.431.

[15] F.G. Blottner, M. Johnson and M. Ellis, "Chemically Reacting Viscous Flow Program for Multicomponent Gas Mixtures," Sandia Laboratories, Albuquerque, NM, USA, SC-RR-70-754, 1971. [Online]. Available: https://www.osti.gov/servlets/purl/4658539, Accessed on: 2025-04-24.

[16] W.G. Vincenti and C.H. Kruger, *Introduction to Physical Gas Dynamics*. Malabar, FL, USA: Krieger Publishing Company, 1965.

[17] B. Armaly, and K. Sutton, "Viscosity of multicomponent partially ionized gas mixtures," in *15th Thermophysics Conference*, Snowmass, CO, USA, 1980. [Online]. Available: doi:10.2514/6.1980-1495, Accessed on: 2025-05-21.

[18] B. Armaly, and K. Sutton, "Thermal conductivity of partially ionized gas mixtures," in *16th Thermophysics Conference*, Palo Alto, CA, USA, 1981. [Online]. Available: doi:10.2514/6.1981-1174, Accessed on: 2025-05-21.

[19] C. Geuzaine and J. Remacle, "Gmsh: a three-dimensional finite element mesh generator with built-in pre- and post-processing facilities," *International Journal for Numerical Methods in Engineering*, vol. 79, no. 11, pp. 1309-1331, Sep. 2009, doi:10.1002/nme.2579.

[20] Oskooi et al., "MEEP: A flexible free-software package for electromagnetic simulations by the FDTD method," *Computer Physics Communications*, vol. 181, no. 3, pp. 687-702, Mar. 2010, doi:10.1016/j.cpc.2009.11.008.

[21] R. Petervari, A. Nekris, and T. Bieker, "Numerical Analysis of Radar-Plasma-Signatures of a Sphere in a Mach 10 Hypersonic Wind Tunnel Flow," in *2021*

18th European Radar Conference (EuRAD), London, United Kingdom, 2021, pp. 86-89. [Online]. Available: doi:10.23919/EuRAD50154.2022.9784578, Accessed on: 2025-05-08.

DEPARTMENT OF PHYSICS
CHALMERS UNIVERSITY OF TECHNOLOGY
Gothenburg, Sweden
www.chalmers.se

CHALMERS
UNIVERSITY OF TECHNOLOGY